BERGISCHE
UNIVERSITÄT
WUPPERTAL

Fachbereich C
Mathematik und Naturwissenschaften

Masterarbeit

Analysis of the discrepancies observed in the stereo and hybrid data in the Pierre Auger Observatory

vorgelegt von

Markus Schauer

aus Heilbad Heiligenstadt

Bearbeitungszeitraum:	06.10.2014 - 06.10.2015
Betreuer:	Dr. Piotr Homola
Erstkorrektor:	Prof. Dr. Karl-Heinz Kampert
Zweitkorrektor:	Prof. Dr. Klaus Helbing

Contents

1 Introduction

The reason why cosmic rays are an extremely interesting topic lies in their potential of having very high energies, which exceed the energies of all known particles on Earth. Although we are hit by a great number of cosmic rays every second, there are still many things we don't know about them. As shown in Chapter 2, primarily their origin and composition are studied along with the energy spectrum and its possible cut-off at highest energies.
After accelerator physics was in the focus of interest for a long time, in the last years astroparticle physics experiments became a more popular topic. The largest and most precise one is the Pierre Auger Observatory which measures air showers, that are cascades of secondary particles, caused by cosmic rays (Chapter 3). In this work, unexplained features are studied which were found in the data of this experiment at highest energies. Could these features be caused by an artifact of the analysis methods or the experiment or even be a result of an unaccounted physical effect? Although this question is not completely answered in this work, the studies that have been done to verify or reject different explanations are presented.
The energy measurements at the Pierre Auger Observatory are performed using different detector techniques: 1660 water Cherenkov tanks and 27 large telescopes detect light to obtain lateral and longitudinal particle distributions. When using both techniques, a hybrid design is formed which is the reason for the high precision of this experiment. Its additional components and enhancements are described in Chapter 4. This work relies on various software packages, especially CORSIKA for simulation studies and the analysis framework $\overline{\text{Off}}\underline{\text{line}}$ which is crucial for the reconstruction of shower events. Both of them and the way the latter reconstructs air showers are explained in greater detail in Chapter 5.
While every detection technique should result in the same reconstructed energy of an event, Chapter 6 demonstrates that this is clearly not always the case. After an extensive motivation the observed features are presented with various cross-checks to confirm their significance. Chapter 7 studies possible origins of these discrepancies, the findings are summarized and discussed in Chapter 8.

2 Cosmic Rays

Like many things in physics, the discovery of cosmic rays happened by accident. In the summer of 1912, the Austrian physicist Victor Hess measured the height dependence of ionization [1]. Using a rising balloon he wanted to demonstrate that the discharges seen in an electroscope are due to radioactive decays in the earth. However, only a weak decrease of ionization could be observed up to a height of 1000 m. Quite the contrary, for increasing heights the measured number of ions increased rapidly, up to a maximum around 4000 m. Hess concluded the existence of highly penetrating particles in the atmosphere which he called "Höhenstrahlung".
Today we know that there are many particles with energies up to 10^{20} eV coming to us from outer space. Since these energies exceed the ones from particles produced at the LHC by many orders, cosmic rays are the most energetic particles observed by humanity and a very interesting and important topic in physics.

2.1 Energy spectrum and sources

The flux of ultrahigh-energy cosmic rays (UHECRs) can be well described by a power law

$$\frac{\mathrm{d}N}{\mathrm{d}E} \propto E^{-\gamma}.$$

This spectral index γ, which indicates a non thermal acceleration mechanism, is not a constant, the steepness of the spectrum changes in various energy ranges as shown in Figure 1. Up to energies of $3 \cdot 10^{15}$ eV, $\gamma \approx 2.7$, then the index changes abruptly to ≈ 3.1. The resulting feature is called "knee" in analogy to a stretched leg viewed from a side. At around $5 \cdot 10^{18}$ eV, the "ankle", the spectrum flattens again and $\gamma \approx 2.7$.
Apparently the flux for low-energy cosmic rays is much higher than for UHECRs (the plot includes more than 30 orders of magnitude), which results in experimental consequences. For energies $\leq 10^{14}$ eV, cosmic rays can be measured by detectors in balloon or satellite experiments. Since the flux of these energies is very high, only a small detection area is necessary and the cosmic rays can be observed directly before they interact with the atmosphere. The *vertical atmospheric depth* $X_\nu = \int \rho \, \mathrm{d}h$ with the density ρ indicates, how much matter was traversed by a particles on its path. One can evaluate the probability of an

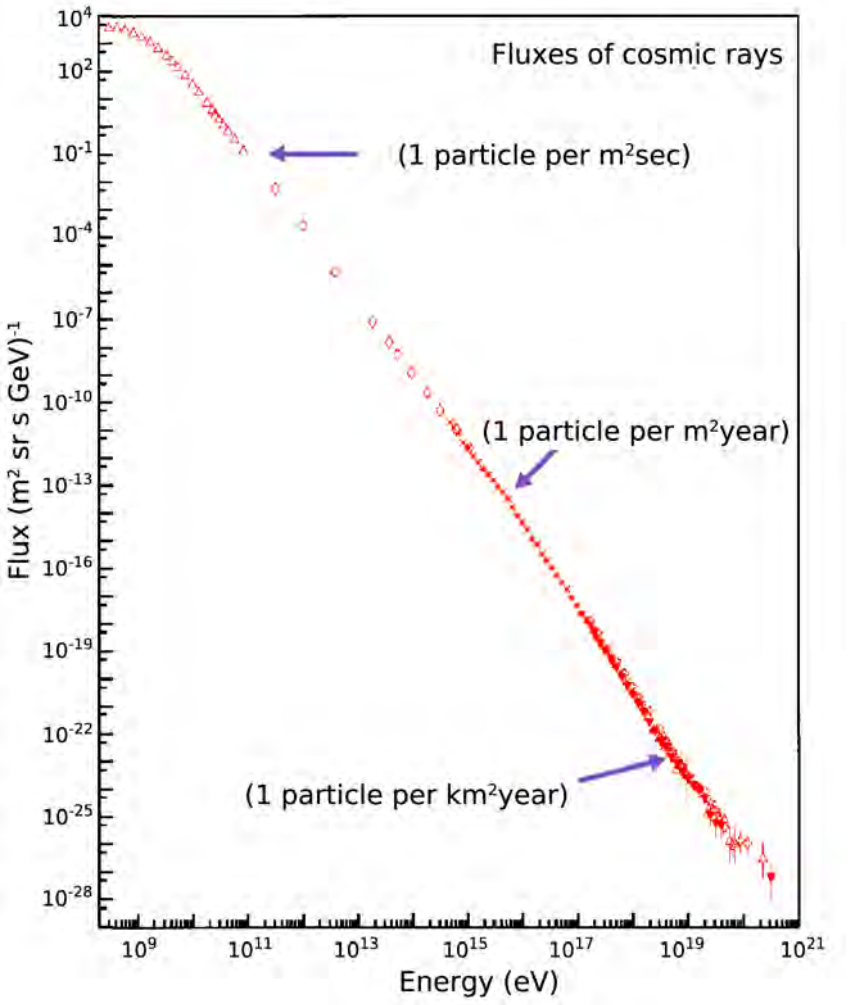

Figure 1: Flux of cosmics rays as a function of energy. One can see the varying steepness of the spectrum and the resulting features, called "knee" (at $3 \cdot 10^{15}$ eV) and "ankle" (at $5 \cdot 10^{18}$ eV). From [3].

interaction by interrelating this with the interaction length

$$\lambda_N = \frac{m_P A}{\sigma_N^{\text{air}}}$$

with the proton mass m_P, the mean mass number of air nuclei A and the interaction cross section σ_N^{air} of a nucleus in air [2]. Since the density of space is very low, any interaction of a particle is unlikely until it reaches the upper atmosphere[1]. However, after progressing to the ground the amount of traversed matter increases significantly, making a direct observation very rare. Rather, the primary particle causes a cascade of secondaries which is called *extended air*

[1]The border between space and atmosphere is usually set at a height of 100 km.

shower (EAS, see chapter 3), so the detection is only indirect. That's the normal case for UHECRs, at high energies the flux is extremely low and thus large detection areas are needed (several thousand km^2), which is only possible at ground level (see chapter 4).
The reason for the different spectral indices, although not fully understood yet, are found in the various sources and possible acceleration mechanisms of cosmic rays as well as miscellaneous propagation effects (e.g. the *Leaky Box model*). While low-energy cosmic rays originate from the Sun, particles with higher energies have to come from the whole galaxy or even beyond. Since most cosmic rays are charged, they interact with the galactic and intergalactic magnetic field. The radius of the resultant circular motion is called *Lamor radius*

$$r_L = \frac{p_\perp}{|q| \cdot B}$$

where q is the charge of the particle and $p_\perp$ the momentum component perpendicular to the direction of the magnetic field which has the strength B. Apparently, r_L increases with energy via $p_\perp$. It follows that for some energy, r_L is large enough to allow the particle leaving the region where the magnetic field acts, in particular the Milky Way. The faster decrease of intensity at the knee energies could be explained by this, since these cosmic rays don't contribute to the measured flux. Consequently, this principle also stands for other galaxies and UHECRs should be able to escape from other galaxies and cross the intergalactic medium to reach the Milky Way. This extragalactic component seems to dominate at the highest energies beyond the ankle, causing the second change of the spectral index. Since high energies result in a high rigidity $R = p_\perp/|q|$, the path of the particle can easier be backtracked to find its source, since it is almost a straight line instead of a curve.
According to current knowledge, astrophysical structures like active galactic nuclei or supernova remnants are responsible for the UHECRs we detect on Earth. In this scenario, the so called *Fermi acceleration* plays an important role: the existence of moving shock fronts with high magnetic fields leads to a stochastic process in which a particle traverses the shock front multiple times due to reflection on magnetic inhomogeneities around the shock front. After each crossing, the particle either escapes or stays in the cycle to be accelerated again by the reflection. Since the escape probability rises with increasing energy, the process turns out to generate a power law spectrum, matching to the measurements. The

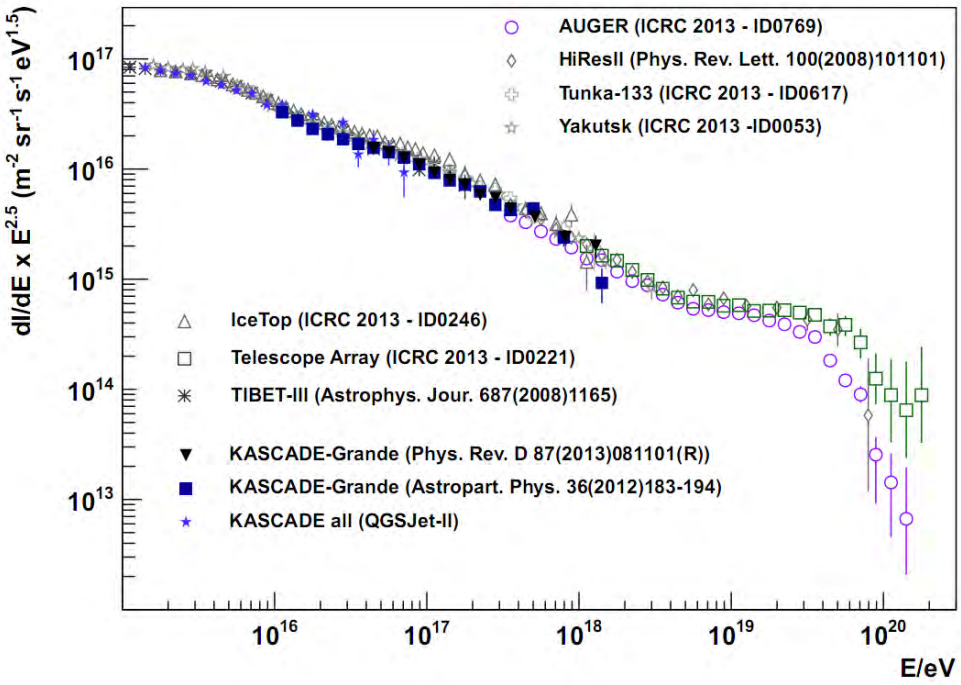

Figure 2: Measurements of various experiments of the cosmic ray spectrum with the prominent cut-off for highest energies (from [4]). To make features better visible, the flux was multiplied by $E^{2.5}$.

energy gain of one crossing is $\propto \beta = \frac{v}{c}$, the velocity of the shock front, hence the distinction as *first order Fermi acceleration*. However, the *second order* Fermi acceleration involves magnetized plasma clouds. The contribution of this process should be smaller since the energy gain is only $\propto \beta^2$ (and $0<\beta<1$).

Figure 2 shows the upper end of the spectrum with measurements of various experiments (e.g. Auger, KASCADE [5], Tunka [6], IceTop [7], TA [8] and HiRes [9]). Further studies [10] showed slight differences of the spectral indices of the various experiments, probably based on different energy resolutions and systematic uncertainties. Apparently there is a flux suppression for energies $> 10^{19.5}$ eV. In 1966 **G**reisen, **Z**atsepin and **K**uz'min predicted this GZK cut-off [11]: protons interact with photons of the cosmic microwave background (CMB) to form a Δ^+ resonance:

$$p + \gamma_{CMB} \rightarrow \Delta^+ \rightarrow p + \pi^0$$

$$p + \gamma_{CMB} \rightarrow \Delta^+ \rightarrow n + \pi^+$$

The protons lose energy (about 20%) due to the formation of the pion until its energy falls below the GZK energy. Due to the mean interaction length of the pion production process this means that highest energies are only possible immediately

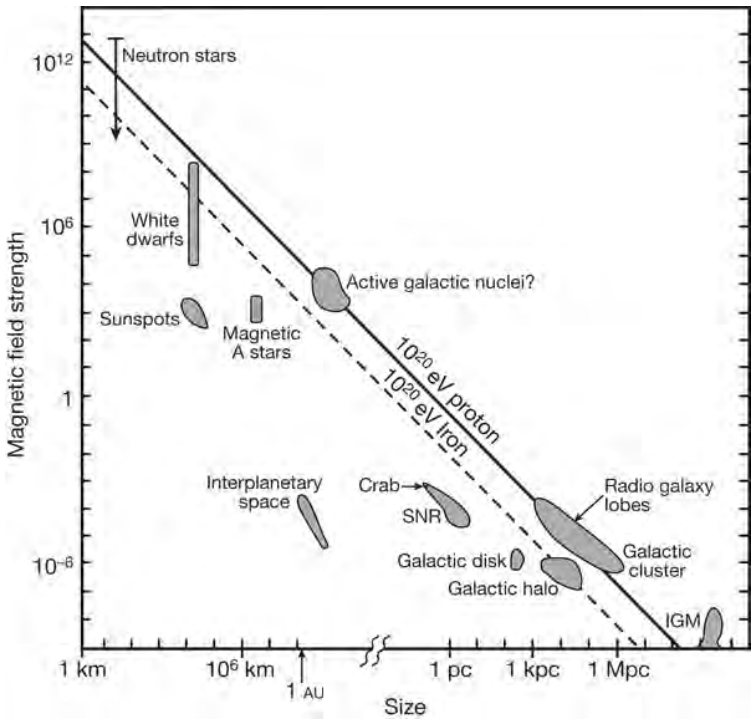

Figure 3: Hillas diagram (from [12]) of possible candidates for the source of UHECRs.

after the acceleration in a horizon of 50 Mpc. The longer the particle travels, the more interactions can occur. Since the cross section of the interaction is energy dependent, only particles above 10^{19} eV are affected. Heavier nuclei also interact with CMB photons, the energy loss is then caused by photodisintegration which means that a single p, n or α is knocked off by the interacting γ, forming a lighter nucleus.

Another possible explanation of the cut-off is based on the famous diagram of Michael Hillas (see Fig. 3). All known astrophysical objects which could be the sources of UHECRs are placed in this plot, the x-axis denotes the size of the accelerating area and the y-axis the corresponding magnetic field strength. The maximum energy after an acceleration depends on these quantities, the charge of the particle $z \cdot e$ and β:

$$E_{\max} \propto \beta \cdot z \cdot e \cdot B \cdot r_L$$

The plot shows that only few objects are capable to accelerate protons to the GZK limit or slightly beyond.

However, the observed cut-off is not a hard one: particles with energies greater than the GZK limit were measured (e.g. the Oh-My-God particle in 1991 with $3.2 \cdot 10^{20}$ eV [13]) and are still puzzling astrophysicists. Due to the GZK effect

these particles should originate in our galactical neighborhood, but there are no sources coinciding with the arrival directions. It seems that there are still some mysteries left to solve.

2.2 Composition

The chemical composition of cosmic rays affects many quantities of the resulting air shower (see chapter 3) and thus can be estimated by interpreting the shower properties. At this point, the composition at highest energies is unknown. Understanding the composition would tell us much about the sources and the propagation of UHECRs. Up to energies of 10^{15} eV the charge of the primary particle is easily determined by direct measurements, which makes drawing precise conclusions of the primary element possible. UHECR events are in turn reliant on indirect experiments: measurements at the Pierre Auger Observatory use the relationship $X_{\max} \propto \lg(\frac{E_0}{A})$, linking the mass number A and the primary energy E_0 with the shower maximum $X_{\max}$ (see chapter 3) and its uncertainty $\sigma(X_{\max})$, to find out whether UHECRs contain light or heavy elements. Fig. 4 shows a comparison between data and simulation. The latter is based on different models and elemental fractions. Both measurements of $<X_{\max}>$ and $\sigma(X_{\max})$ show an agreement. Near the ankle region ($10^{18.0}$ eV$-10^{18.3}$ eV) lighter nuclei seem to dominate. For higher energies, however, the data points approach the iron lines, making a heavy nuclei composition probable. At this point, a mixed composition

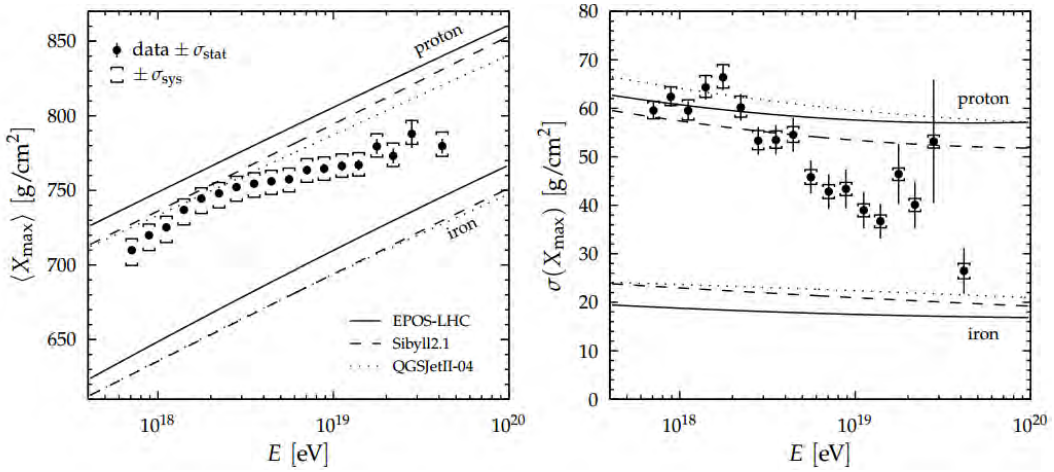

Figure 4: $<X_{\max}>$ and $\sigma(X_{\max})$ measurements in comparison with air shower simulations for highest energies. Different lines indicate different hadronic interaction models for pure proton or iron compositions (from [14]).

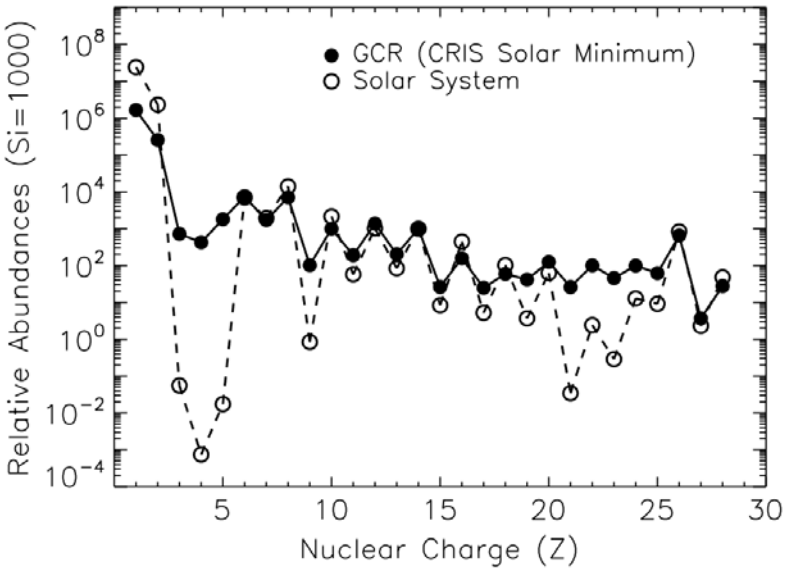

Figure 5: Comparison of abundances seen in cosmic rays and the solar system for lower energies ($E = 10^8$ eV) (from [15]).

theory is favored.

Most of the stable elements of the periodic table are found in cosmic rays with lower energies, but are the abundances of the individual elements the same as in our solar system? Fig. 5 shows a comparison of these abundances around energies of $E = 10^8$ eV. For most elements, only small differences occur, but there are also some notable exceptions. Li, Be and B (Z=3,4,5) show a strong overabundance in cosmic rays. These elements are hardly seen in the solar system because they are the result of spallation of C and O after interacting with the interstellar medium. The same explanation holds for the overabundance of the subiron elements (Z=21-25), being the spallation product of iron. Moreover, the ratio of even to odd Z elements is systematically lower for galactic rays, a result of the weaker bound between odd Z nuclei.

3 Extensive Air Showers

In 1938, Pierre Auger proved the existence of *extensive air showers* (EAS) by measuring coincidence rates of detectors hundreds meters apart in the Alps [16]. Like already stated, UHECRs can not be measured directly. An indirect detection is possible, since the primary particle hits eventually an oxygen or nitrogen atom of the atmosphere. The same is also true for the resulting secondary particles, thus after a few interaction lengths a cascade of particles is formed - also called air shower.
The main goal when studying air showers is the reconstruction of the primary particle and its properties based on the measured values (see chapter 5). This primary can be a photon, a proton or a heavier nucleus. Even neutrinos or more exotic particles are not excluded. Due to the high energy of most primaries, the air shower moves almost with the speed of light c, forming a slightly curved shower front. When passing through the atmosphere, the air shower develops along the *shower axis*, which is described by the extended path of the primary. This allows one to differ between two important profiles: the longitudinal profile shows usually the number of particles N or the deposited energy along the track segments $\frac{\mathrm{d}E}{\mathrm{d}X}$ versus the slant depth X which is simply

$$X = \frac{X_\nu}{\cos\theta}$$

with θ as the zenith angle of the shower. The aforementioned quantity $X_{\max}$ is defined as the depth at which N is at maximum. On the other hand, the lateral distribution shows the particle density along the plane perpendicular to the axis. Both profiles are needed for a successful shower reconstruction.

3.1 Shower components and development

A typical EAS consists of three different components which are able to blend into each other via decays and interactions: Protons, neutrons, pions and kaons form the **hadronic component**, which is characterized by a high ionization rate. Pions and kaons evolve into the other components, depending on their charge. *Neutral* pions have a branching ratio of 98.8% for decaying into two photons. These can only interact electromagnetically which leads to a cascade composed of electrons, positrons and photons, forming the **electromagnetic**

(EM) component. The EM component is the numerically largest group and its particles carry approximately 90% of the energy of the whole shower. Since they can easily be absorbed by the atmosphere, it's also called soft component. The hard or **muonic component**, however, is able to penetrate the atmosphere due to the high energies and masses of the muons, originating from the decays of *charged* pions. Muons have only a small lifetime of $\approx 10^{-6}$ s, but their energies are high enough for time dilation effects and as a consequence they are able to reach the ground.
To parameterize the number of particles in an air shower at different depths X, the *Gaisser-Hillas function* [17]

$$N(X) = N_{\max} \left(\frac{X - X_0}{X_{\max} - X_0} \right)^{\frac{X_{\max} - X_0}{\Lambda}} \exp\left(\frac{X_{\max} - X}{\Lambda} \right) \tag{1}$$

is normally used where X_0 and Λ denote two fit parameters (besides $X_{\max}$ and $N_{\max}$). The former two are usually identified as the starting point of the shower and the shower decay length respectively. The Gaisser-Hillas fit is applied to the measured profile to get the shower maximum. Lastly, the shower age s is defined as

$$s = \frac{3X}{X + 2X_{\max}}.$$

Thereby this parameter is in the range from 0 to 3, reaching $s = 1$ at $X = X_{\max}$.

3.2 Heitler model

A simple model introduced by Heitler in 1944 [18] allows a rough description of the basic properties of an air shower. In this model, starting with a primary with $E = E_0$, after passing one interaction length λ two new particles are created which each have the energy $E = E_0/2$. Hence, after each λ, the number of particles doubles while their energies are halved. Fig. 6 shows the principle for an electromagnetic shower. The relevant processes are pair production ($\gamma \rightarrow e^- e^+$) and bremsstrahlung ($e^\pm \rightarrow e^\pm \gamma$).

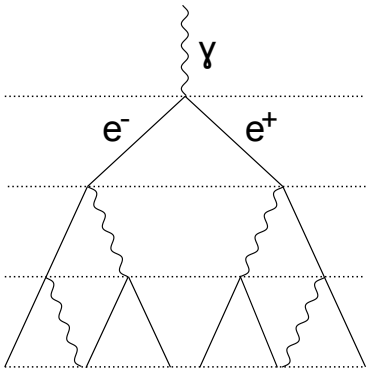

Figure 6: Heitler model

The shower reaches $N_{\max}$ as soon as the energies of the secondaries fall below the

critical energy E_c. At this point no new particles can be created, because ionization losses become more important than radiation losses. For electromagnetic showers, this happens around 85 MeV. The corresponding depth $X_{\max}$ which can be calculated by

$$X_{\max} = \lambda \cdot \frac{\lg(\frac{E_0}{E_c})}{\lg(2)} \tag{2}$$

and the number of particles at shower maximum is

$$N(X_{\max}) = N_{\max} = \frac{E_0}{E_c}.$$

The superposition principle states that a nucleus with the mass number A creates a similar shower as A proton primaries with $E = \frac{E_0}{A}$ per proton. Thus

$$X_{\max} \propto \lg(\frac{E_0}{A})$$

and it becomes obvious how important the measurement of $X_{\max}$ is in respect to determine the type of the primary particle.

3.3 Fluorescence light

To detect the light of an EAS, two physical effects are used: emission of fluorescence and Cherenkov light. Since they are indistinguishable at the detector, one has to know the ratio between the two to get a good reconstruction of the primary particle. By measuring light from both effects with different detectors the reconstruction quality can be even increased. The following clarifies the physical background, for the specific setup at the Pierre Auger Observatory to measure the light, see chapter 4.

The majority of secondary particles are electrons and positrons which lose their energy by ionization and molecular excitation. The latter relates primarily to N_2, as it's the main component of the atmosphere. After remaining in the excited state for about 10 ns, deexcitation causes the emission of fluorescence light in the UV range. The strongest emission is between $\sim 300{-}400$ nm, thus in this range the detectors have the highest efficiency (among others, due to filter transmissivity and photomultiplier quantum efficiency) [19]. Fig. 7 shows the UV fluorescence spectrum for N_2 with the corresponding bands in this range.

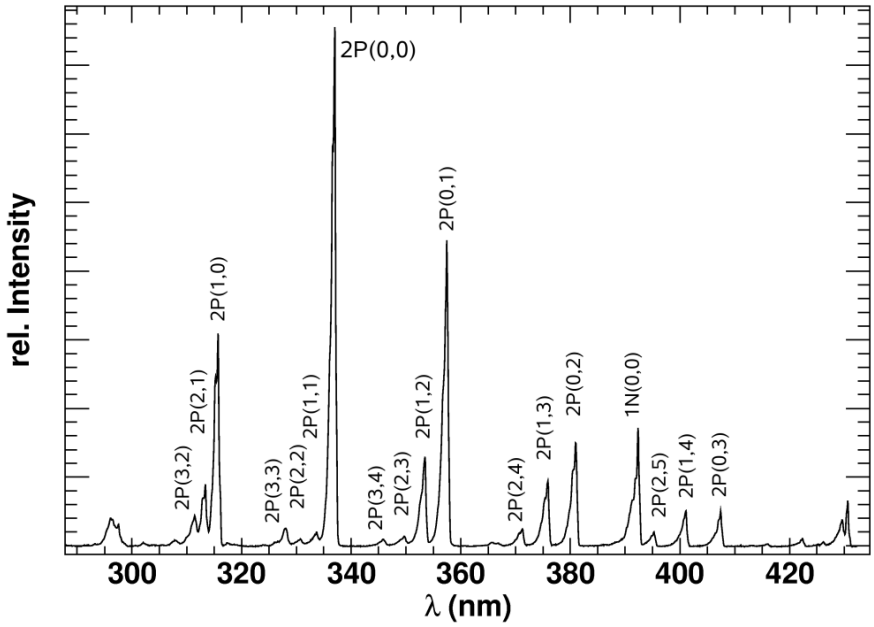

Figure 7: UV fluorescence spectrum for N_2 measured by the AirFly experiment (from [21]).

The number of emitted photons depends proportionally on the deposited energy, moreover fluorescence light is usually emitted isotropically. Since the light signal is very weak, the night sky background (NSB) has to be as low as possible to measure a shower, thus nights around new moon are preferred. For the same reason, this technique allows only the detection of primary particles with energies $E > 10^{16}$ eV. The number of emitted fluorescence photons per slant depth and wavelength is given by [20]:

$$\frac{\mathrm{d}^2 N_f}{\mathrm{d}X \mathrm{d}\lambda} = \int Y(\lambda, p, T, u, E_e) \cdot \frac{\mathrm{d}N_e(X)}{\mathrm{d}E} \cdot \frac{\mathrm{d}E_{dep}}{\mathrm{d}X} \cdot \mathrm{d}E \tag{3}$$

with the energy spectrum of the electrons $\frac{\mathrm{d}N_e(X)}{\mathrm{d}E}$ at an atmospheric depth X, $\frac{\mathrm{d}E_{dep}}{\mathrm{d}X}$ denoting the energy deposited in a layer of atmosphere with thickness $\mathrm{d}X$, and the fluorescence yield Y which describes how many photons were emitted per deposited energy at a wavelength λ. Y is depending on the atmospheric pressure p, the temperature T, the humidity u and the electron energy E_e.
Since the measured light originates from different heights the signal helps greatly gauging the longitudinal profile.

3.4 Cherenkov light

Additionally to fluorescence, Cherenkov light reaches the detector. An important difference between these signals is that Cherenkov light is not emitted isotropically, but instead beamed in forward direction forming a distinctive cone with opening angle ϑ. The well studied mechanism of Cherenkov radiation was discovered in 1934 by P. Cherenkov. As sketched in Fig. 8, a passing charged particle causes a partial polarization in a dielectric medium which is symmetrical. Accelerated charges result in electromagnetic waves which leads to interference. In the normal case ($v < \frac{c}{n}$ with the refractive index of the medium n) there is a destructive interference and no macroscopic radiation occurs. For higher velocities though ($v > \frac{c}{n}$), the polarization is not symmetrical anymore and constructive interference causes the radiation of Cherenkov light.

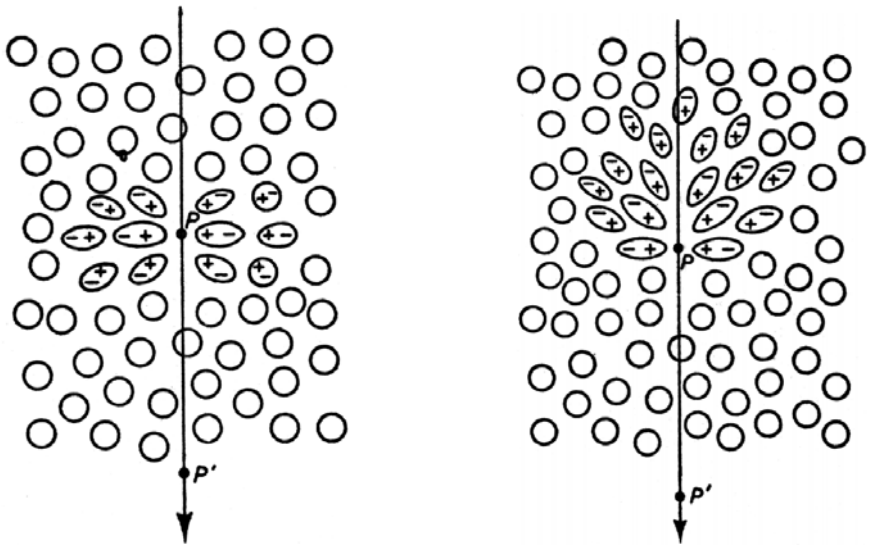

Figure 8: Polarization due to a charged particle at different velocities. Left: $v < \frac{c}{n}$, right: $v > \frac{c}{n}$ (from [22]).

A simple Huygens construction (for example in ref. [23]) shows the relation

$$\Theta = \arccos\left(\frac{1}{n\beta}\right)$$

with the angle of the Cherenkov cone Θ and $\beta = \frac{v}{c}$. The Cherenkov condition $v > \frac{c}{n}$, or $\beta > \frac{1}{n}$, means that apparently there is a minimum energy for the

Cherenkov effect. It can be calculated by [24]

$$E_{\min} = \frac{mc^2}{\sqrt{1-n^{-2}}}, \tag{4}$$

thus an electron in the atmosphere has to have an energy of at least 20.7 MeV to emit Cherenkov light.
The angular distribution of Cherenkov light can be approximated by [25]

$$\frac{\mathrm{d}N}{\mathrm{d}\Omega} \propto \frac{e^{\vartheta/\vartheta_0}}{2\pi \sin\vartheta}, \quad \vartheta_0 \simeq 4.5^\circ.$$

The amount of Cherenkov photons N_c is given by [26]

$$\frac{\mathrm{d}N_c}{\mathrm{d}X} = \frac{2\pi\alpha z^2}{\rho(h)} \int_{\lambda_1}^{\lambda_2} \frac{1}{\lambda^2} \cdot \left(1 - \frac{1}{(n(\lambda)\beta)^2}\right) \cdot \mathrm{d}\lambda \tag{5}$$

with the fine-structure constant α=1/137, z as the charge number of the traversing particle and the atmospheric density ρ. To detect Cherenkov light in the atmosphere, moonless nights are required again. Since the refractive index n is very small for air, the opening angle Θ is of the order of $1^\circ - 1.5^\circ$ and increases for lower altitudes due to the denser atmosphere. Because of this narrow cone, the Pierre Auger Observatory detectors are usually not hit *directly* by Cherenkov light. However, as most of the photons are scattered, they are seen outside of the cone and reach the detector nevertheless. As a consequence, scattered light forms a significant contribution to the signal and should be understood in the best possible manner. A distinction is made between *Rayleigh* and *Mie* scattering, the former one is an elastic scattering process with particles much smaller than the wavelength of the participating photons. The attenuation of a beam with N photons depends strongly on the wavelength [25]:

$$\frac{\mathrm{d}N}{\mathrm{d}x} \propto -\frac{N}{\rho} \cdot \frac{1}{\lambda^4}$$

i.e. photons with small wavelengths are much more attenuated. The angular distribution

$$\frac{\mathrm{d}\sigma}{\mathrm{d}\Omega} \propto 1 + (\cos\vartheta)^2$$

shows that the intensity of Rayleigh scattered photons is at maximum in forward and backward direction.
Mie scattering, on the other hand, is the process of light scattering on aerosols

which are small dust or dirt particles in the atmosphere of the same size order as the photon's wavelength. The attenuation

$$\frac{\mathrm{d}N}{\mathrm{d}x} \propto -N \cdot e^{-h/H_M}, \quad H_M = 1.2 \text{ km}$$

depends mainly on the corresponding altitude h. Since most aerosols are at lower altitudes, only there a significant attenuation occurs. Mie scattering is forward peaked:

$$\frac{\mathrm{d}\sigma}{\mathrm{d}\Omega} \propto e^{-\vartheta/\vartheta_M}, \quad \vartheta_M = 26.7°.$$

Especially at lower altitudes the aerosol density has a significant impact on the shower reconstruction and thus its type has to be measured exactly.
Moreover, multiple scattering can occur for a photon, but a distinction from other components is not possible.
At the Pierre Auger Observatory, for the detector monitoring the atmosphere, direct and scattered Cherenkov light is only the background of the wanted fluorescence signal and therefore has to be subtracted to estimate the correct shower energy, since the reconstruction of primaries at this detector is based on fluorescence.

3.5 Anisotropic re-emission of fluorescence

Cosmic ray experiments like at the Pierre Auger Observatory consider only isotropic emission of fluorescence light, i.e. any additional possible fluorescence effects are neglected.
In this regard, an interesting fact is that Cherenkov light can be absorbed by atmospheric N_2 molecules. Nitrogen shows a very strong absorption of photons with wavelengths between $80 - 100$ nm (Tanaka-Worley band) [27], a range in which the amount of Cherenkov photons is roughly thrice than in the detection range $(300 - 400$ nm) due to the $\frac{1}{\lambda^2}$ behavior of $N_c(\lambda)$ (see eq. 5). The question is how much of the absorbed energy is re-emitted as light and how does the angular distribution look like. Excitation of a molecule is only possible, if the molecule has a special alignment to the E-field vector of the light (photoselection).
Fig. 9 clarifies the concept of photoselection: δ_A is the angle between $\vec{E}$ and the absorption transition moment. The latter is a measure of the ability for an atom or molecule to absorb or emit electromagnetic radiation. The transition moment is a vector, which direction indicates the required polarization, while the square of

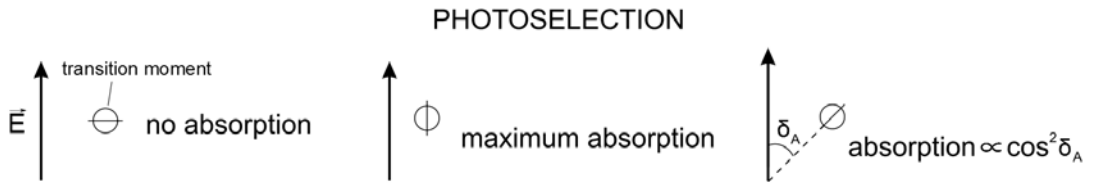

Figure 9: Photoselection: for absorption $\vec{E}$ and the transition moment have to be aligned (from [28]).

its absolute value corresponds to the probability of the respective process. Hence, the more $\vec{E}$ and the transition moment are aligned, the more likely becomes an absorption, i.e. if incident Cherenkov light is polarized, only molecules with a special alignment are able to absorb.
In the case of Cherenkov photons, $\vec{E}$ is parallel to the polarization vector which is perpendicular to the Cherenkov cone. Cherenkov light is naturally 100% radially polarized [30]. While a shower evolves through the atmosphere, the polarization of Cherenkov photons decreases due to scattering of electrons. After reaching the ground, at core distances around 125 m, which is the standard radius of a proton induced Cherenkov cone, still 30% remain [29]. As seen in Fig. 10 data and simulations agree for showers with $E > 10^{17}$ eV: the polarization decreases for smaller radii since light observed at the axis has to be unpolarized [31] and

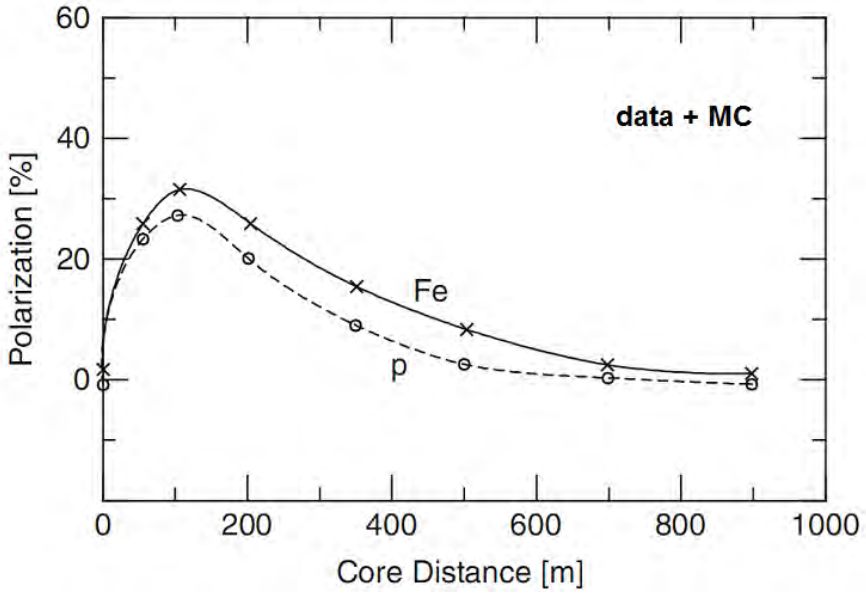

Figure 10: Data and Monte Carlo of the polarisation dependence on core distance for proton and Fe induced air showers (from [29]).

for larger distances because these particles are heavily scattered. The maximum is as predicted at $120 - 130$ m.
While iron induced showers exceed proton showers in polarization, ref. [30] declares a polarization of even 45% for photon showers.
This means, air molecules with special alignment are indeed being excited by polarized Cherenkov light and the distribution of their emission moments is anisotropic. Ref. [28] states: "Because the distribution of excited fluorophores is anisotropic, the emitted fluorescence is also anisotropic". The resulting anisotropy $r(t)$ would behave like

$$r(t) = \frac{I_{\parallel}(t) - I_{\perp}(t)}{I(t)} = \frac{3\overline{\cos^2 \delta_A(t)} - 1}{2} \tag{6}$$

with $I_{\parallel}(t)$ and $I_{\perp}(t)$ as the light intensities parallel and perpendicular to the direction of propagation. This anisotropy would be unaccounted in the current model. If the effect is nonnegligible, the models used presently underestimate the light flux that reaches detectors. Thus, further studies are needed.

4 Pierre Auger Observatory

The Pierre Auger Observatory is currently the worldwide largest detector array in astrophysics. Proposed in 1992 and completed in 2008, the Observatory started data taking already in 2004. To avoid urban background light, the site is located in the province Mendoza in the Argentinian Pampas.
The purpose of the experiment is the detection of cosmic rays between energies of $10^{17} - 10^{20}$ eV, studying their composition, spectrum and possible sources by looking at their arrival direction. Like shown in Fig. 11, the experiment is composed of two different detectors: the Surface Detector Array (**SD**) counting particles on the ground and the Fluorescence Detector (**FD**), looking into the atmosphere over the SD. Both detectors track UHECRs with independent methods. It allows a hybrid reconstruction of EAS properties which reduces the uncertainties, in

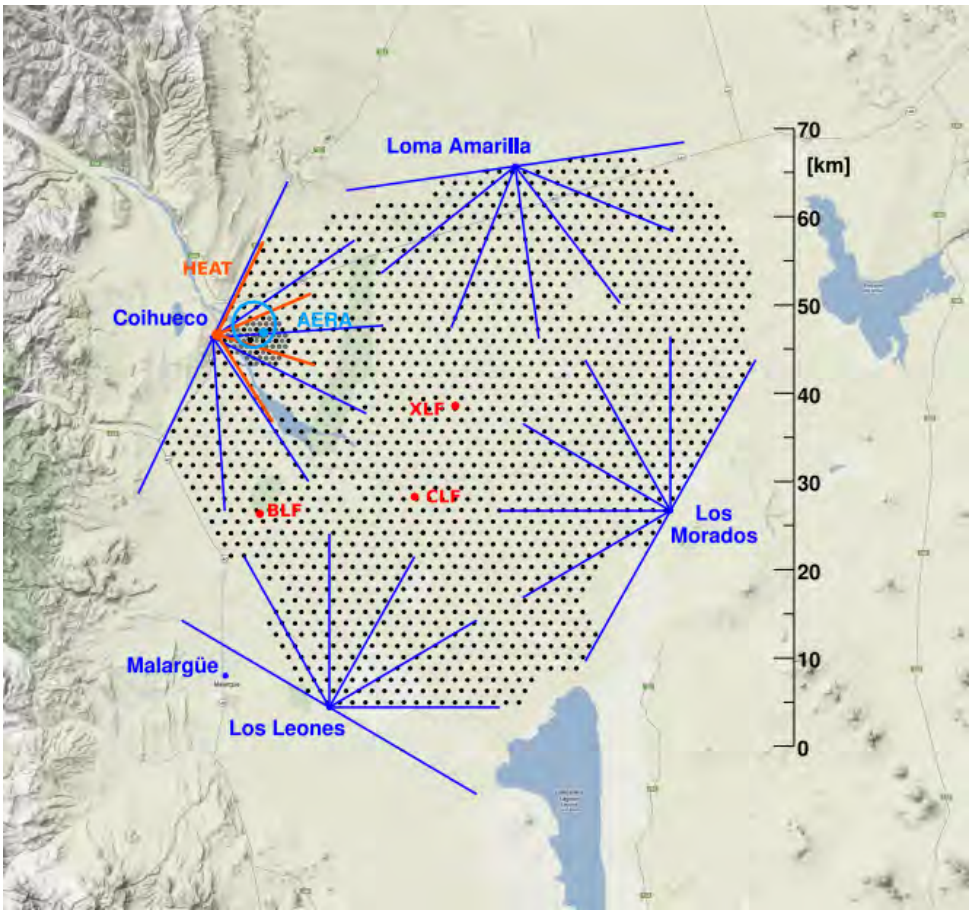

Figure 11: Map of the Pierre Auger Observatory. Besides the SD (black dots) and the four sites of the FD one can also see auxiliary facilities like XLF and enhancements like HEAT (from [32]).

particular those of the total energy and shower geometry. More than 500 physicists from nearly 100 institutes around the world are working together on this project.
As stated, monitoring the atmospheric conditions is necessary for a correct EAS reconstruction. Aerosols have a strong effect on the transmission of light in the atmosphere and thus should be measured precisely. Therefore, they are measured at different frequencies by two laser facilities, XLF and CLF (extreme and central laser facility). The latter shoots 50 laser pulses with a width of 7 ns every quarter-hour vertically in the sky with a wavelength $\lambda = 355$ nm. Atmospheric scattering generates tracks which are similar to the ones caused by an EAS and can be distinguished by specific GPS timing. Laser light should be attenuated in the same way as fluorescence light and hence can be detected at the FD [33]. Thus with the scattered intensity the vertical aerosol optical depth (VAOD) can be measured in dependence on the height h, indicating the transparency of the atmosphere. For this, the measured laser profiles are compared with a reference clear night profile which is annually selected. The VAOD is unitless and defined as

$$\mathrm{VAOD(h)} = -\frac{\ln(\frac{N_{obs}(h)}{N_{ref}(h)})}{1 + \csc\chi}$$

with the number of photons N_{obs} from the measured laser profile, the number of photons N_{ref} from the reference night and χ as the elevation angle of the camera for the corresponding laser track segment. Next, differentiating VAOD(h) returns the extinction coefficient α(h) which has to be re-integrated to get the final VAOD value for the corresponding FD station. A polluted sky results in a large value, making a successful shower reconstruction more difficult.
Another laser system (LIDAR) monitors the cloud coverage and additionally there are cloud cameras installed at the various FD buildings. A description of the two main detectors and important enhancements of the experiment follows.

4.1 Surface Detector Array

The aim of the SD is the measurement of EASs by using water Cherenkov tanks. The detection in the SD doesn't take place in the atmosphere, but as the name suggests, on the ground. To this end, there are 1600 stations (Fig. 12) uniformly distributed with a distance of 1500 m to each other on an area of 3000 km^2 [34]. This large area is needed to compensate the low flux of UHECRs and get

Figure 12: Left: SD station, Right: one of the FD sites, Loma Amarilla.

nevertheless a statistical significance of the collected data. Each station contains highly purified water with a resistivity of 15 MΩ cm. The water container (with a 3.6 m diameter and a height of 1.55 m) is surrounded by a highly reflective polyethylen shell, preventing light from the outside to enter. Each station is powered autonomously by a solar panel and has a battery for the nighttime. The electrons and muons of air showers penetrate the shell and emit Cherenkov light in the water. Since water has a higher refractive index than air, a velocity of only $0.75c$ is sufficient for the Cherenkov effect. Three photomultiplier tubes (PMTs) are installed to measure any signal. Together with the time stamps the signal records are sent to the Central Data Acquisition (CDAS). Due to the apparent lack of a significant environmental influence the SD stations work also during the day and thus the SD has a duty cycle of almost 100%.

Since the detection takes place on the ground, only a statement about the lateral EAS profile is possible, as the SD doesn't see the longitudinal development of a shower. The energy reconstruction with the SD only underperforms in comparison to the FD, but within the concept of a hybrid reconstruction it gives an accurate energy measurement (see chapter 5.3). The more energy a shower contains, the more particles cover a larger area at low altitudes, thus the cone has diameters range between 500 and 5000 m. The SD detects all events with $E > 3 \cdot 10^{18}$ eV. Additionally, there are infilled stations near one of the FD stations (Coihueco) with only half the distance (750 m) between them to measure events with lower energies (10^{17} eV) which don't cover that much ground.

For the calibration of the SD atmospheric muons are used, since they form an uniform and very well understood background. To avoid background particles during the analysis of air showers, several triggers exist [35]: e.g. the time over threshold trigger (ToT) catches the electromagnetic part of the shower which is

more spread out in time, in this way single muons are rejected. To identify an air shower, a combination of signals clustered in space and time is used [36]. On the last level, the T5 trigger accepts only events with a high accuracy in the reconstruction of the core position and energy. The events used in this work have passed this trigger.
The reconstructed energy at the SD, E_{SD}, is determined by a cross calibration with E_{FD}, the reconstructed energy from the FD. Different energies are measured at various SD stations with different distances to the core, thus a fit can be applied. As the SD energy estimator the shower size parameter $S(1000)$ is used, the expected signal at a distance of 1000 m from the shower core, corrected for attenuation effects [37]. $S(1000)$ is converted to the reference parameter S_{38}, which is the signal $S(1000)$ the shower would have with an arrival direction of 38° in zenith angle. The size parameter is related to E_{FD} via the power law

$$E_{\mathrm{FD}} = A \cdot S_{38}^{B}.$$

Since hybrid events are used for the calibration, E_{FD} is known and a fit returns $A = 0.190 \pm 0.005$ EeV and $B = 1.025 \pm 0.007$ for vertical showers [38], hence S_{38} grows approximately linearly.

4.2 Fluorescence Detector

On the other hand, the FD (Fig. 12) measures the longitudinal development $\frac{\mathrm{d}E}{\mathrm{d}X}(X)$ by looking for fluorescence and Cherenkov light in the atmosphere. Integration of the $\frac{\mathrm{d}E}{\mathrm{d}X}(X)$ profile gives the dissipated electromagnetic energy, which is approximately 90% of the primary's total energy. The FD is located at four different sites: Los Leones (LL), Los Morados (LM), Loma Amarilla (LA) and Coihueco (CO), surrounding the SD. Each site has a building with six FD bays each. In every bay there is a Schmidt telescope, all six telescopes combined are often called an "eye". Through a UV glass filter, light with a wavelength between 290−410 nm enters the bay (for the transmission coefficient of the filter see Fig. 13), then it is reflected by a segmented spherical mirror with a surface of 10 m^2, which focuses the collected light on a camera in the center of the aperture [35]. In Fig. 14 the schematics of a FD building and the functional principle of a telescope are depicted. The camera consists of 440 PMTs which record photons with a frequency of 10 MHz. To avoid a

signal loss, the gaps between the PMTs are filled with small light reflectors. Each PMT can be seen as a pixel which covers a field of view (FOV) of $1.5° \times 1.5°$, its signal is read out via ADC (analog-to-digital-converter).

The whole telescope has a viewing range from $1.5° - 31.5°$ in elevation, thus vertical showers with a small θ will only be seen partially since the FD looks rather over the ground than up in the sky. Each site covers a 180° range in azimuth. A shutter system closes the bays during the day and full moon so that the PMTs don't receive too much light which might cause a damage. Hence, the duty cycle is strongly restricted to about 14%.

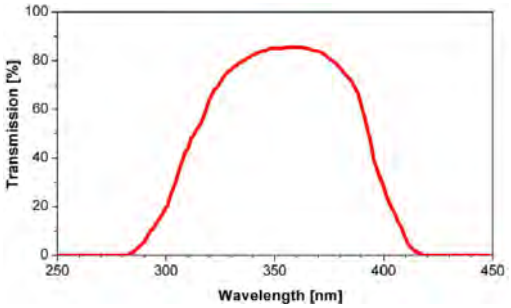

Figure 13: Transmission coefficient of the used UV filter (from [35]).

Interesting events are selected by various triggers. As a first condition a signal in a pixel has to exceed a specific threshold. A search for designated patterns of neighboring pixels (like a straight line) follows, which would indicate an air shower. A powerful trigger is the hybrid one, T3. After a preliminary reconstruction of the shower based on its direction, the core position at the ground is estimated. If there is an corresponding signal in the SD, the event is sent to the data acquisition (DAQ).

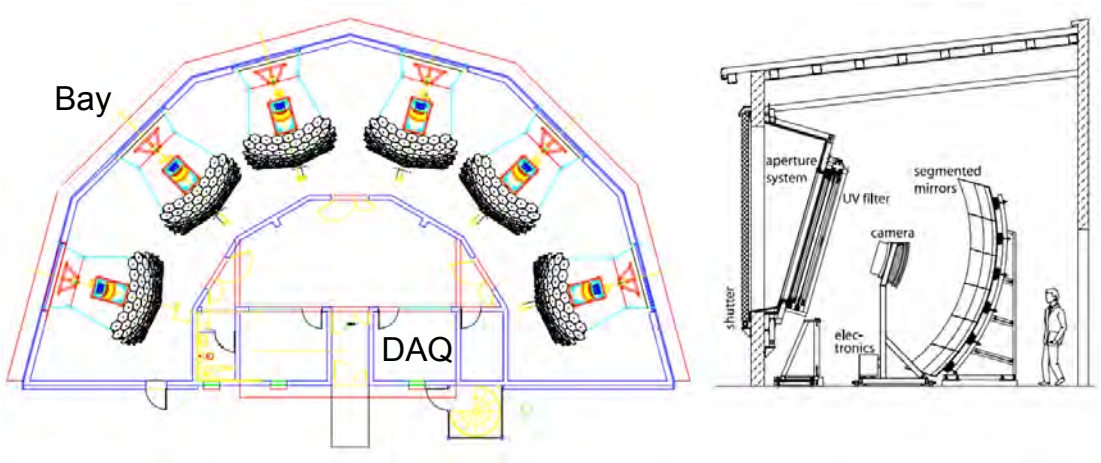

Figure 14: Left: schematic layout of a FD building, Right: setup of a single telescope (from [35]).

4.3 Enhancements

Beyond the basic detectors, several enhancements were installed at various locations at the Pierre Auger Observatory to study specific properties of UHECRs. Near Coihueco the High Elevation Auger Telescopes (HEAT) [39] were built. With three telescopes a fifth eye is formed. It has a higher data read-out rate (20 MHz) than the other eyes and started stable data taking in 2010. HEAT operates in two different modes: in downward mode, it works like a standard eye and is used for calibrations and cross-checks of the near Coihueco station. Using the upward mode, HEAT shows its value with a FOV elevation range from $31.5° - 61.5°$. This way, low energy events between $10^{17} - 10^{18}$ eV can be studied, an interesting energy range in which supposedly the transition between galactic and extragalactic UHECRs occurs. These low energy showers emit only small photon fluxes and can only be seen when near an FD site. However, since they also develop earlier and high in the atmosphere, the tilted orientation of the telescopes is needed for observation. HEAT looks directly up in the atmosphere and thus sees much more direct Cherenkov light than all other eyes. HEAT in the upward mode is usually combined with CO to form the virtual eye HeCo. The advantage is shown in Fig. 15. While CO wouldn't be able to observe $X_{\max}$ by itself, together with HEAT the whole shower is recorded.

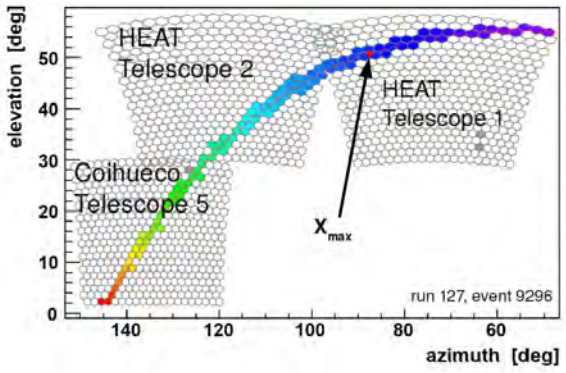

Figure 15: Combined FOV of CO and HEAT telescopes (from [39]).

Another PAO extension is the Auger Engineering Radio Array (AERA) [40]. 124 antennas measure coherent radio emission of EAS in the $10 - 100$ MHz range. The dependence of radio emission on shower parameters and geometry is studied and composition measurements in the transition region with very high precision are possible [41]. While having a duty cycle of almost 100%, AERAs first measurements confirmed the theoretical predictions that were made about the emission mechanism [42].

5 Simulation and Reconstruction

To understand the data as good as possible, comparisons with simulated events are needed. The better sub-processes like absorption, particles decays, traversing the atmosphere or the deflection in the magnetic field are considered, the more these sets can help with respect to the data. While most sub-processes are indeed comprehended, the combination of them and the arising effects making things difficult. The biggest issue is that current interaction models have to be extrapolated for highest energies, thus introducing larger uncertainties. Simulations are an important field and described in the following along with the subsequent reconstruction algorithms.

5.1 CORSIKA

CORSIKA (Cosmic Ray Simulations for Kascade) [43] is based on the Monte Carlo method and uses RMMARD as random number generator. It's written in Fortran 77/90 and was first published in 1989. With CORSIKA, the evolution of a shower through the atmosphere to the ground is simulated, taking into account the key effects like the emission of Cherenkov light.
When performing a simulation one has to choose between several hadronic interaction models for low and high energies, however the MC set used in this thesis is using EPOS LHC, EPOS 1.99, QGSJet II.03, QGSJet II.04 as well as Sibyll 2.1 as high energy interaction models and different primary particles like protons, He, O and Fe nuclei.
It is important to decide how precise shower simulations should be: particle showers can become very complex since a 10^{20} eV shower can contain 10 sub-showers with $E = 10^{19}$ eV each, or 10^6 sub-showers with 100 TeV, 10^{11} sub-showers with 1 GeV and so on. Thus the simulation of every secondary particle would be too time consuming and a *thinning* method is applied. Below a specific energy threshold multiple particles are combined to one particle with an appropriate weight w. The important configurable parameters are $\eta_{\mathrm{th}} = E_{\mathrm{th}}/E_0 = 10^{-6}$, with the energy threshold, E_{th}, the initial energy, E_0, and the maximum weight, $w_{\mathrm{max}} = 1700$. All desired parameters are set in the steering card before the simulation starts, in appendix A.1 one can find an example card with a short description of the various parameters.
When using CORSIKA for events recorded at the Pierre Auger Observatory, one

has to take particular care of the different definitions of coordinate systems (see Fig. 16). While CORSIKA's x-axis points to the geomagnetic North, the Auger Collaboration defined the x-axis in the geographical East. Thus a rotation of +90° is required and additionally the magnetic declination has to be considered. For the last years, it has been around 2° in Mendoza [44], but since it is time dependent the correction has to be modified regularly.

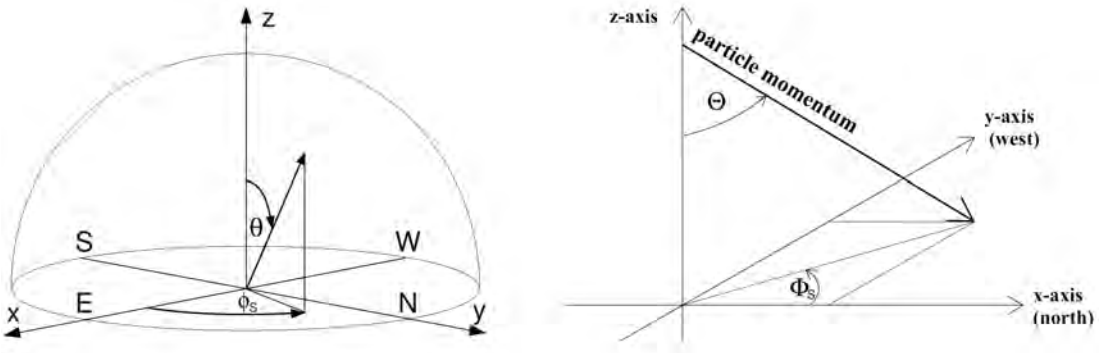

Figure 16: Definitions of the coordinate systems for the Pierre Auger Observatory (left) [45] and CORSIKA (right) [43]. For the former the x-axis points to geographical East, for the latter to geomagnetical North. Θ identifies the zenith, ϕ_S the azimuth.

5.2 Offline

For the analysis of the measured data the Pierre Auger Collaboration developed a software framework which suits its specific needs. This framework is called Offline, and it's written in C++ to take advantage of object oriented design. In this work the version v3r0p0 is used, its ensuing description follows Ref. [46].
The main purpose is the reconstruction of air showers based on the detected raw data of SD, FD and hybrid events. Furthermore, for MC showers a simulation of the detector's response is feasible. The standard output format after the reconstruction, called ADST (Advanced Data Summary Tree) [47], is based on ROOT. For looking at reconstructed events directly, the graphical interface EventBrowser is implemented. As shown in Fig. 17, there are three parts of the Offline framework: Detector description, modules containing the main algorithms and Event Data. A task like the reconstruction of an event is handled by processing a whole sequence of modules which contain algorithms. Offline was designed in a way that it is easy to write or modify a module by yourself. It simply has to be registered in the framework. Due to using XML files the exchange of various

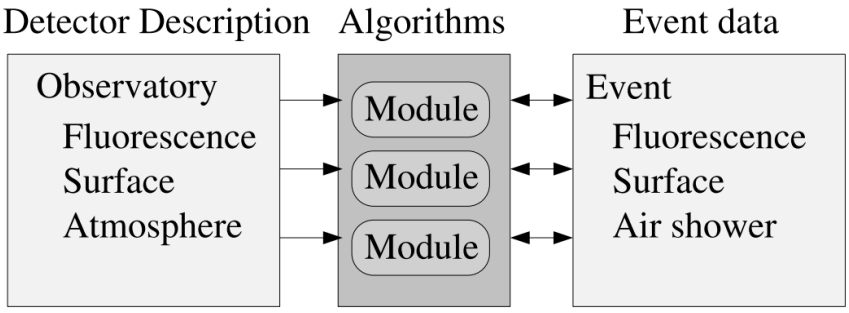

Figure 17: The three main components of the Offline framework, modules containing algorithms, the Event Data and the Detector Description (from [46]).

algorithms is possible without recompiling the executable every time. Modules read information from the Detector Description and from the Event data, process it and write the results back into the Event Data. The Detector Description contains the configuration of the detector, its performance within a specific time, and the atmospheric conditions. While static information is stored in XML files, slowly varying data (like calibration data) can be found in MySQL databases. A request of data is passed to a registry of managers which extract only a specific sort of information each. The Event Data contains all the raw, reconstructed or simulated data.
Parameters of the modules like cut thresholds can be changed easily in XML files. The main configuration file is the *bootstrap file*. It comprises the location of the used module sequence, the list with the input files and manual overrides, where necessary. Thus the name of the bootstrap file is usually the only needed input option when executing Offline on the command line.

5.3 Shower reconstruction

The modules used for a standard shower reconstruction are explained in the following. In the beginning the module *EventFileReaderOG* reads the raw data or, alternatively, the output from simulations like CORSIKA. Then, *EventCheckerOG* rejects damaged events with missing information which could hinder the reconstruction.
By using *FdCalibratorOG* the measured signals are converted into counts of photons based on the calibrations from the MySQL database. In the next step, *FdPulseFinderOG* identifies for each pixel the time with the maximum amount

of detected photons. This is the time at which the shower crosses the FOV of this pixel. After knowing the arrival time for each pixel the background has to be suppressed. This is done with *PixelSelectorOG* by rejecting isolated pixels, regarding time and space.

At this point the light collection is completed and there is enough information to reconstruct the geometry of the shower. *FdSDPFinderOG*'s task is to find the **shower detector plane** (SDP), which contains the shower axis and the telescope (see Fig. 18) by using all pixels with signal pulses. The normal vector $\vec{n}$ defines the SDP and is obtained by minimizing

$$\chi^2 = \sum_{i}^{\text{pixels}} |\vec{n} \cdot \vec{r_i}|^2 \cdot w_i,$$

with the pointing direction $\vec{r_i}$ of pixel i and its weight w_i which simply depends on the amount of photons the pixel sees. The found SDP can be described by its inclination, ϑ_{SDP}, and its azimuth, φ_{SDP}. Other important parameters are R_p, the perpendicular distance between telescope and track, and t_0 which is the time when the shower front passes at R_p from the detector. Moreover, χ_0 is the angle between the ground and the shower axis within the SDP. To get the shower

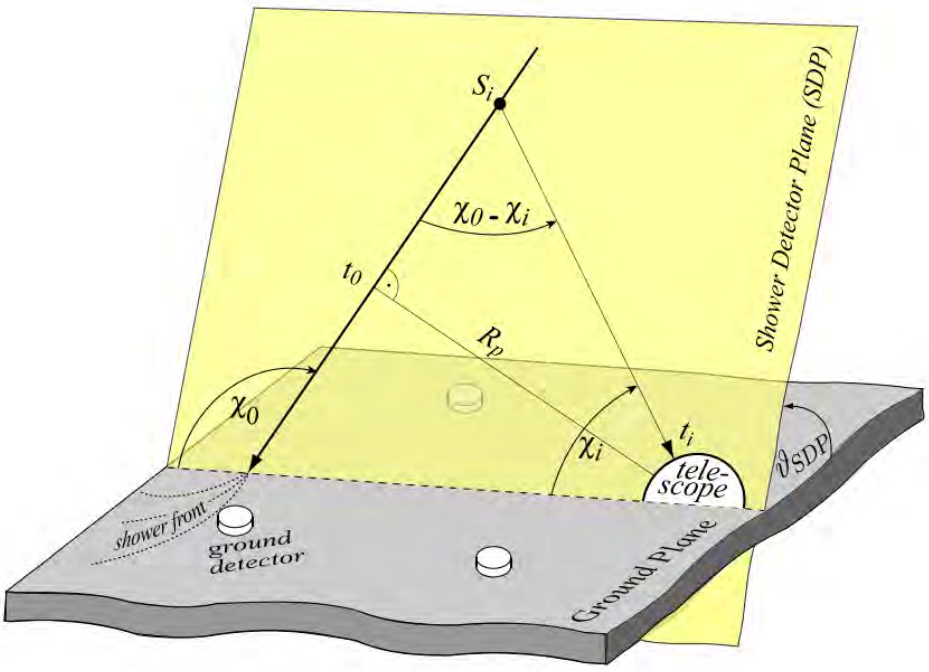

Figure 18: Geometry of an air shower, the various parameters are explained in the text (from [35]).

axis *FdAxisFinderOG* is utilized. With the obtained timing information, to every point on the shower axis S_i a detection angle χ_i and the arrival time t_i at the detector can be assigned:

$$t_i = t_0 + \frac{R_p}{c} \tan\left(\frac{\chi_0 - \chi_i}{2}\right).$$

In the module *HybridGeometryFinderOG* the advantage of using two different detection techniques comes into effect. It looks for an SD station close to the SDP. With the combined timing information of a SD station and a FD camera a fit is possible to determine the direction and position of the axis more precisely than with FD alone. The hybrid reconstruction has a precision of 50 m in the core position [35] and 0.5° in calculating the shower direction [48].
After getting the light yield for each shower point at a specific slant depth X_i in the first part and determining the geometry in the second, one is now interested in the longitudinal profile of the energy deposit. This is done in *FdApertureLightOG*. Since the shower geometry is known, calculating the attenuation of the light due to scattering in the atmosphere is possible. There are different parametrizations of the lateral and angular distribution of Cherenkov and fluorescence light which give the expected number of direct and scattered photons for each shower segment. The derivation is following Ref. [49]: For direct fluorescence, with the fluorescence light yield Y_i^f, the amount of produced photons in the slant depth interval ΔX_i is

$$N_\gamma^f(X_i) = Y_i^f \frac{\mathrm{d}E}{\mathrm{d}X_i} \Delta X_i. \tag{7}$$

The emitted light is distributed isotropically over a sphere with the surface $4\pi r_i^2$ with the distance to the detector r_i. Since there is attenuation the detection efficiency ϵ is less than one and only a fraction of light T_i is detected. With the factor

$$d_i = \frac{\epsilon T_i}{4\pi r_i^2}$$

the fluorescence light flux which is measured at the FD telescopes is

$$y_i^f = d_i Y_i^f \frac{\mathrm{d}E}{\mathrm{d}X_i} \Delta X_i. \tag{8}$$

In a similar way, the expected flux of Cherenkov light can be calculated. For direct Cherenkov light it is

$$y_i^{Cd} = d_i f_C(\beta_i)\ Y_i^C N_e(X_i)\ \Delta X_i \tag{9}$$

with the electron and positron number $N_e(X_i)$ above the specific energy threshold, as these particles are the source of Cherenkov light (details on the Cherenkov light production in Sec. 3.4). $f_C(\beta_i)$ is the fraction of Cherenkov photons emitted at an angle β w.r.t. the shower axis and the yield Y_i^C includes inter alia the height dependent energy threshold. For scattered Cherenkov light a model is used which describes the number of photons in a beam at X_i as the sum of all Cherenkov light produced at all previous depths X_j, attenuated from X_j to X_i by T_{ji}. Hence, the light yield is

$$y_i^{Cs} = d_i f_s(\beta_i)\ \sum_{j=0}^{i} T_{ji} Y_j^C N_e(X_j)\ \Delta X_j. \tag{10}$$

The total light seen by the detector at t_i is the sum of all the partial light yields:

$$y_i = y_i^f + y_i^{Cd} + y_i^{Cs}.$$

To gain the energy deposit, the matrix notation is used. Then the total light yield can be written as a vector $\vec{y}$ with the i-th component y_i and the wanted energy deposit as another vector, $\vec{w}$, with the i-th component $\mathrm{d}E/\mathrm{d}X_i$. $\vec{w}$ is related to $\vec{y}$ by the **Fluorescence-Cherenkov Matrix** C:

$$\vec{y} = C\vec{w}. \tag{11}$$

By comparison of Eqs. 8, 9 and 10 one gets the following structure of C:

$$C_{ij} = \begin{cases} 0, & i < j \\ c_i^d + c_i^s, & i = j \\ c_{ij}^s, & i > j \end{cases}$$

with the abbreviations

$$\begin{aligned} c_i^d &= d_i(Y_i^f + f_C(\beta_i)Y_i^C/\alpha_i)\Delta X_i \\ c_{ij}^s &= d_i f_s(\beta_i) T_{ji} Y_j^C/\alpha_i\ \Delta X_i \end{aligned} \tag{12}$$

and $\alpha_i = \frac{\mathrm{d}E/\mathrm{d}X_i}{N_e(X_i)}$. With inversion of this matrix the solution for the energy deposit is:

$$\hat{w} = C^{-1}\vec{y} \tag{13}$$

and can be solved numerically. Typically not all of the shower is visible within the limited FOV of the FD. This is why *FdEnergyDepositFinderKG* performs a Gaisser-Hillas fit (see Eq. 1) to the reconstructed w_i to get the complete profile of energy deposit. Through the integration of this profile one obtains the calorimetric energy, which has to be corrected for invisible energy (of neutrinos that hardly interact with matter) to get the total energy of the primary particle. This is achieved by the module sequence mentioned above. The energy resolution is 14% [38], statistical uncertainties are derived from a full propagation of all event-by-event uncertainties. Systematic uncertainties are caused by the fluorescence yield, the atmospheric model, the telescope calibration and the reconstruction process [48]. In the end, *RecDataWriterKG* writes the output as an ADST file.
With the help of the aforementioned *EventBrowser*, one simulated example event is illustrated in figure 19a. As an hybrid triple event, it is observed by three FD telescopes (LL, LM and CO) as well as by 24 SD stations. The size of each circle indicating a station is proportional to the measured signal, the 1σ contour marks the core position. This event has a zenith angle of 58.6° and an azimuth of 0.4°. While the reconstructed X_{max} is at 779 g/cm^2 the energy was calculated by LL to be $2.17 \cdot 10^{19}$ eV. How the longitudinal energy deposit profile is reconstructed by LL is shown in Fig. 19b. The characteristic distribution is plotted along with the Gaisser-Hillas fit (red line). The red dot marks the depth of X_{max}. Figure 19c demonstrates how the measured light at the telescope can be divided into its different sources. While the biggest part (white) belongs to fluorescence light, this event has with 19% a higher Cherenkov light fraction than the average (about $5 - 10\%$). While direct Cherenkov light (red) peaks at the same time as fluorescence light, scattered light (blue and green) is delayed due to the longer track length. In Fig. 19d one can see the triggered pixels of a camera. The color code of the signal specifies the time, going from cold to hot. Grey pixels were triggered with a bad timing, while black ones were rejected during the shower axis determination. This axis is indicated by the red line. In a similar way Fig. 19e shows at which time and at which χ angle a signal was detected. The SD station with the largest signal is used for the hybrid reconstruction, it is marked by the black square.

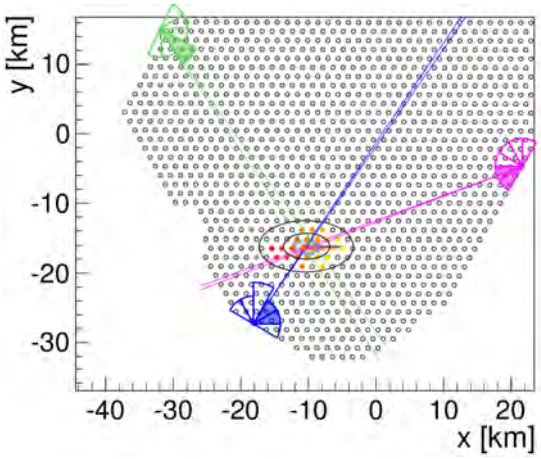

(a) Geometry of a simulated example event

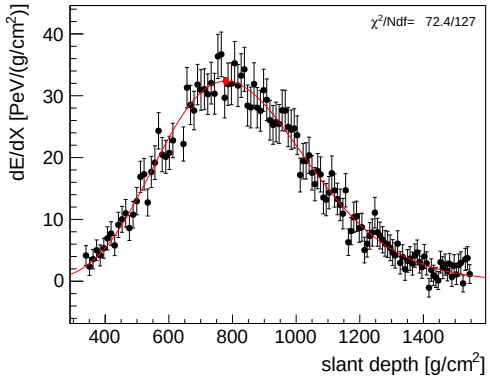

(b) Energy deposit profile

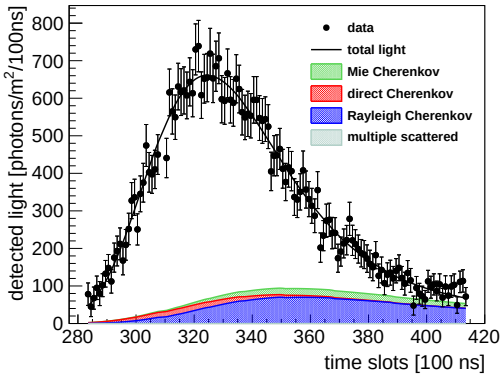

(c) Profile of light components

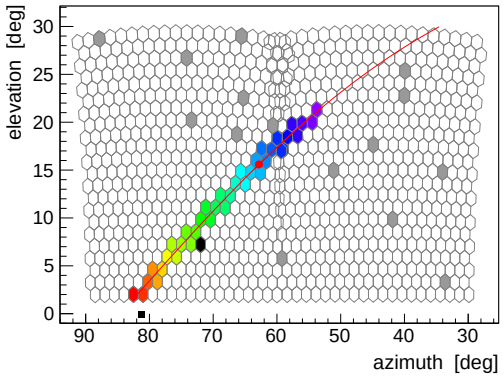

(d) Track in a camera

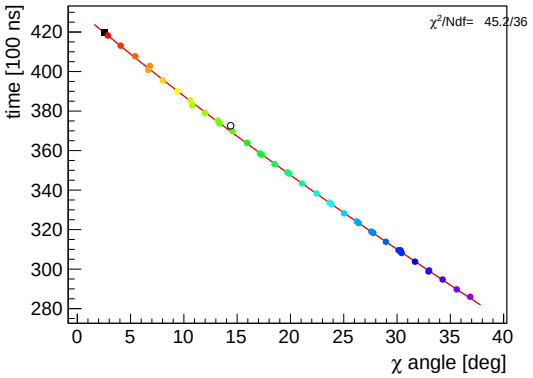

(e) χ vs. t plane

Figure 19: Simulated example event with various profiles measured by the FD station Los Leones. See description in the text.

6 Unexplained features in the data

This and the following section present the analysis of the found peculiarities in the data. After the motivation of the analysis, some definitions and preliminary considerations, the observed features are presented along with first cross-checks. As sufficiently described, the Pierre Auger Observatory, as the leading UHECR research project, uses two different detection techniques to obtain the energy of an observed air shower. Multiple FD eyes are able to detect photons emitted due to various physical processes. With the hybrid concept air showers can be reconstructed precisely and the energies of both detectors, E_{FD} and E_{SD} can be calculated. To test the hybrid technique the consistency of these energies can be checked: on average, they should be equal. However, due to calibration these two quantities are interconnected and for a reliable comparison one studies stereo events instead, which also return two energies. These energies are independently reconstructed by two separate eyes and should be also equal. As it turned out, though, significant discrepancies were noticed [50, 51] which can not be explained by the Cherenkov asymmetry [52] (see Sec. 6.3). This work aims at understanding the source of this disagreement in energy reconstructing by studying various qualities of this feature.

6.1 Preparations

To avoid confusions in the later parts of the analysis, commonly used terms have to be introduced. An important quantity regarding the geometry of an air shower is the *viewing angle* θ_{v}, that can be defined for each point on the shower axis. It is the angle between the shower axis and the line of sight to the eye which is also called the *viewing vector*. As the shower approaches the ground the angle widens. The viewing angle at the time the shower reaches the FOV of the eye is called *minimum* viewing angle (θ_{vm} in Fig. 20a). Naturally it is smaller for inclined showers. Since these showers can look into the FOV depending on their orientation, more (direct) Cherenkov light is able to reach the eye. This is shown in Fig. 20b. Large Cherenkov fractions (including both direct and scattered light) are caused by small minimum viewing angles and for larger angles the amount of Cherenkov light drops significantly. The discrepancy between data and simulation should be noticed, this will be taken up again in later sections.

In this work several data sets were used which are described in the follow-

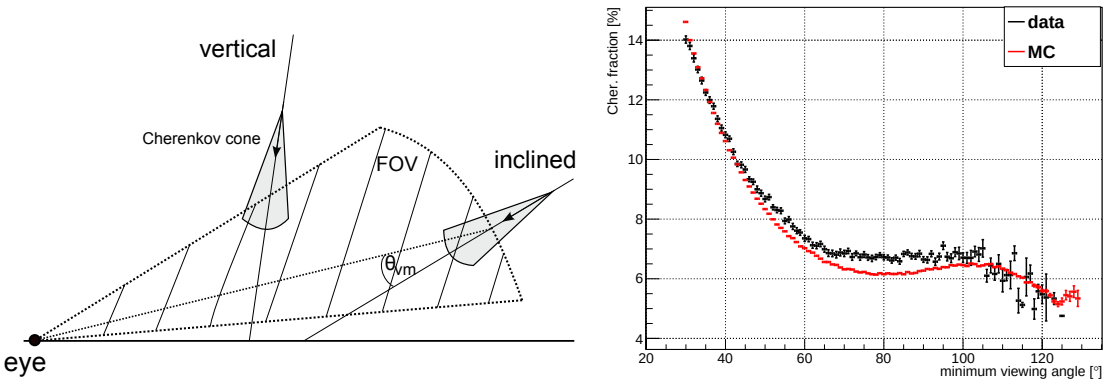

(a) (b)

Figure 20: (a) Geometry of vertical and inclined showers and definition of the minimum viewing angle θ_{vm}. (b) Relation between total Cherenkov fraction and minimum viewing angle using the LongXmax and Naples set (introduced in the text).

ing. Most plots are based on the LongXmax set [14], which applies specific cuts on all data in the time period 2004−2012. It contains almost 20000 high quality events and is currently the best possible Auger collection to get an unbiased X_{max} distribution. The used cuts are listed in appendix A.2, which also contains an explanation of the most important ones. Precuts ensure that only time periods with good data taking conditions are used, moreover, only high-energy events are accepted (E>$10^{17.8}$ eV). Quality and fiducial cuts aim at a precise X_{max} determination with minimal distortions. An important cut rejects all events with a minimum viewing angle <20°. Thus the LongXmax cuts reject the events with the largest Cherenkov fractions. The reason is that the Cherenkov fraction falls exponentially with the viewing angle and even small uncertainties in the geometry can cause large changes in the reconstructed energy. During the analysis it was tried temporarily to omit this cut to get cherenkov-rich events, but to be most convincing the original cuts remain untouched for the following analysis.
To access specific events occasionally additional cuts for subsets are used. The *golden hybrid* set contains around 2000 LongXmax events with a very high reconstruction quality. Only hybrid events with high energies (E>$10^{18.5}$ eV) and small zenith angles (θ<60°) are allowed. The *stereo* set contains events which were detected by at least two different eyes. The drawback of this set is its size with only 181 events. Therefore, one last set is introduced, consisting of almost *4000 stereo* events which were measured by the observatory between 2005 and 2013 and thus

representing the largest possible stereo set. On the one hand, due to the application of almost no cuts these events are expected to have a lower quality. On the other hand this also means there is no θ_{vm} cut, which makes Cherenkov-rich events accessible. To ensure a certain quality only the cut $\sigma_E/E < 0.2$ is applied with the energy reconstruction uncertainty σ_E. To be detected by two or more eyes an air shower has to have a high energy and since more light is collected than in a mono event, the energy uncertainty is usually rather small which results in the end in a reasonable quality of the data set. That is why it is used to support plots based on the LongXmax set. Later shown plots (see Sec. 6.3) justify this decision.

6.1.1 Issues with the used Monte Carlo set

As mentioned before, simulated events are also needed for comparisons with the data. The question has arisen, which MC set would be the most sensible to use. Producing own MC sets in CORSIKA with desired input parameters was successful, but the available computing resources allowed only performing a limited number of simulations and reconstructions, thus the needed statistics were not achievable due to time. Instead, the most reasonable options were either using official Grid sets produced by the Simulation Committee of the Pierre Auger Collaboration or the recently published shower library from Naples [53]. In the end, the latter was used. With simple ROOT trees the Naples library introduces a different file format (instead of the common ADST files) which requires some code adjustments. In return, the 2.5 million events are easy accessible and much more compact than in an ADST file. The downside is the loss of some information, for example the specific Cherenkov components (like Rayleigh or Mie scattered fractions) of an event. The filesize of the library is only 2.2 GB, while comparable ADST files would be significantly larger. After the LongXmax cuts around 600.000 events remained. Only 300.000 of these events could be processed due to limited hardware, this shouldn't introduce any bias, though.
However, towards the end of the analysis it turned out that there was a mistake made in the setting of the simulation reconstruction. As shown later, this work contributed in finding this issue. For a systematic study, the telescope properties were measured with an isotropic point-like source in a way that only one pixel would be illuminated [54, 55]. At this point it was discovered that there was an optical halo around the mainly hit pixel. Thus, 14% of the total intensity didn't

reach this pixel. This optical halo is primarily caused by the reflectivity of the PMT surface [56] and is also influenced by sub-processes like Rayleigh scattering. Usually only light in a certain angular range around the SDP is used for a reconstruction and the lost light is corrected for [57]. This correction was implemented with a data-driven parametrization [58]. Since the effect is not completely understood yet it cannot be excluded that the parametrization introduces inconsistencies in other areas. Reconstruction of data requires the option *eSpotGroup2* in the `opticalhalo` settings to correct for this effect, which results in an increase of 8% in the reconstructed energy. Since the halo isn't simulated, the correction has to be switched off when reconstructing MC sets (option *eNone*) to prevent overreconstruction. This was forgotten not only for the official Grid productions, but also for the Naples set since it uses the same settings. Therefore, for some time there was no correctly reconstructed official MC set with the latest official release with which a large production of MC sets was done (version v2r9p3) available. The request for the reconstruction of a new set with the correct settings was made and it is in the approval process within the Collaboration.
Since this bug was found late in my analysis, the lack of time and computing resources inhibited the production of an own set with the required size. Thankfully, the Naples group reacted fast and finished the re-reconstruction of their library with correct settings two weeks before the end of my analysis and thus I am able to use high-quality MC events nonetheless. Before this new set, the older ones allowed only less convincing statements due to the additional energy shift, an problem which is now avoided.
Another issue which effects all MC sets has to be adressed: for simulated events the SD energy calibration is not valid under all conditions. This is caused by the correlation of the SD energy estimator with the shower maximum $X_{\max}$. While data sets are calibrated in a way that the energies of the FD and SD agree, minimum-bias cuts like the FOV cut reject certain shower maxima and thus energies, and a bias is introduced [59]. This is demonstrated in Fig. 21 which contains two scatter plots of the FD and SD energies. For showers with protons as primary particle (Fig. 21a) this issue is clearly visible. The green line indicates how an agreement in energy would look like while the red one is an actual fit of the data. Especially in the high energy range the SD apparently reconstructs lower energies than the FD, since events with high energies in SD are rejected due to the corresponding $X_{\max}$. However, for iron induced air showers the data points agree much better (Fig. 21b). Since the shower maxima of these events

are located higher in the atmosphere they are not rejected and the calibrations works.
The final MC set which is used for this analysis contains p, He, O and Fe as primary particles which results in a total shift of SD energies that has to be scaled as a consequence. Only hybrid MC plots are affected because for stereo events only FD energies are used.

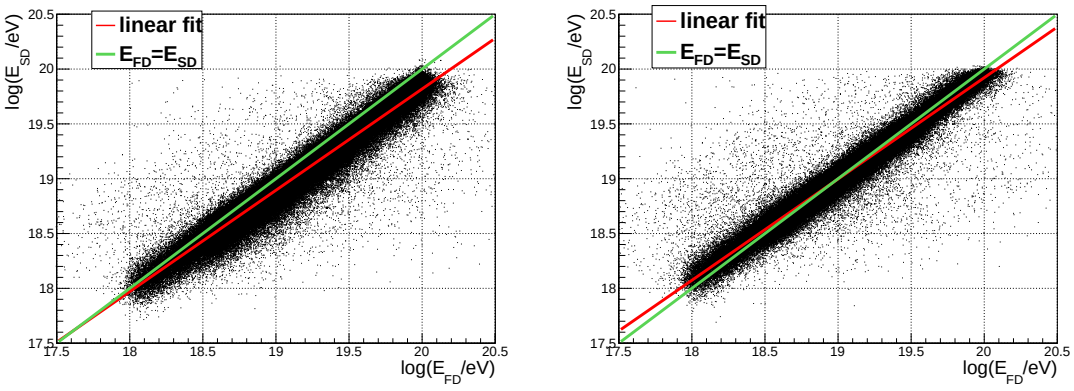

Figure 21: Comparison of the agreement between FD and SD energies for a pure (a) proton and (b) iron subset of the Naples shower library. While the green line represents $E_{\mathrm{FD}} = E_{\mathrm{SD}}$, the red line fits the data points linearly to show differences between the trends.

6.2 The Cherenkov asymmetry

This work is inspired by Ref. [60] which studies a parametrization of the Cherenkov asymmetry (explained below in more detail). Both Ref. [60] and this work rely heavily on the angle ϕ which mustn't be confused with the shower azimuth ϕ_S. For the exact definition of this angle one has to consider the shower plane, i.e. the plane perpendicular to the shower axis. The magnetic field vector, $\vec{B}$, and the viewing vector of the line of sight from the eye $\vec{c}$, which points from the photon emission point to the FD eye, are projected onto the shower plane and include ϕ (see Fig. 23b). The calculation and implementation of ϕ was cross-checked independently using various methods. The method used for this work is explained in the following: for the implementation in the code determining ϕ, $\vec{B}$ was hardcoded at the beginning and later calculated accordingly to the IGRF

model [61]. The calculation of $\vec{c}$ requires the use of spherical coordinates:

$$\vec{c} = \begin{pmatrix} \cos(\phi_{SDP} + \alpha)\sin(\theta_{SDP}) \\ \sin(\phi_{SDP} + \alpha)\sin(\theta_{SDP}) \\ \cos(\theta_{SDP}) \end{pmatrix},$$

with the SDP coordinates (see chapter 5.3) and the backwall angle α for each telescope, which describes its orientation w.r.t. the Earth's magnetic field. Using the vector of the shower axis, $\vec{n}$, the projection of $\vec{B}$ and $\vec{c}$ is easily obtained, e.g. for $\vec{B_T}$:

$$\vec{B_T} = \vec{n} \times \left(\frac{\vec{B} \times \vec{n}}{\|\vec{n}\|^2} \right).$$

To get ϕ in the desired range [0°:360°] the atan2 function has to be used:

$$\phi = \text{atan2}(\sin\phi, \cos\phi),$$

with

$$\sin\phi = \frac{\|\vec{c}_T \times \vec{B}_T\|}{\|\vec{c}_T\| \cdot \|\vec{B}_T\|}$$

and

$$\cos\phi = \frac{\vec{c}_T \cdot \vec{B}_T}{\|\vec{c}_T\| \cdot \|\vec{B}_T\|}.$$

From the definition of ϕ it is obvious that each eye is only able to see a restricted range due to its different orientation. This is shown in Fig. 22a. For example LL sees vertical showers ($\theta < 60°$) between $60°-240°$ and inclined ones at the outer borders of this range. When looking at total numbers (Fig. 22b), a lack of events in the regime of LM is evident. This is also caused by the FD layout, the range between $250°-270°$ is the only one which is only covered by one eye.

In Ref. [60] the angular distribution of Cherenkov light is studied closely. Several parametrizations of the angular distribution existed already at this point, but all of them considered the distribution approximately symmetric with respect to the shower axis [62, 63] and depending on the viewing angle, θ_v. However, charged particles ($e^{\pm}$) which emit Cherenkov light are deflected by the geomagnetic field, an effect which was neglected until then. This deflection leads to a charge separation and instead of considering only an angular dependence on θ_v for the number of Cherenkov photons, the above explained angle ϕ must be also taken into account. Before this ϕ dependence was considered there was a significant over-

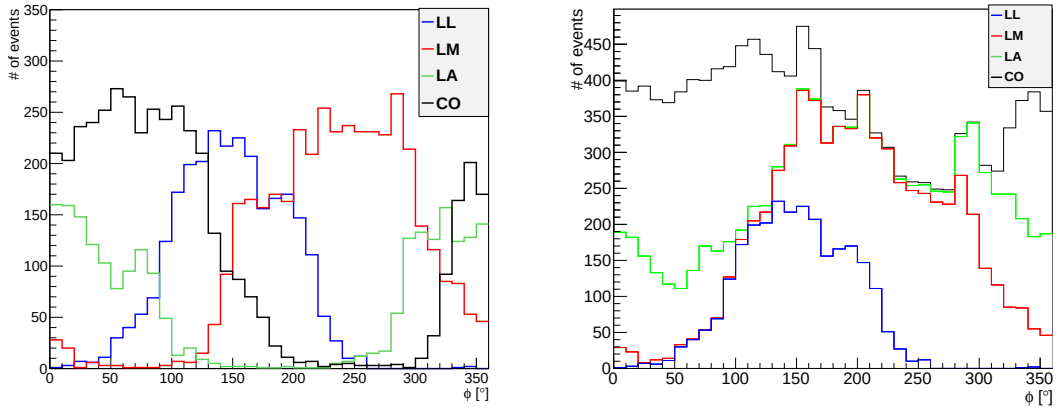

Figure 22: (a) Simple ϕ distribution showing the observed ranges for each individual eye using the LongXmax data set. (b) The stacked distribution shows the total number of events for each ϕ, indicating a lack of events with angles between 200°−330°.

/underestimation of light for specific ϕ ranges. The resulting parametrization for an example configuration is depicted in Fig. 23a. Due to the magnetic field lines, there are two favored directions for photons, one peak at 90° (for light emitted from e^-) and one around 270° (for e^+ based photons). The different heights can be explained by the different amount of e^- and e^+ in the shower. The effect should be most pronounced for large B_T and small air densities. The

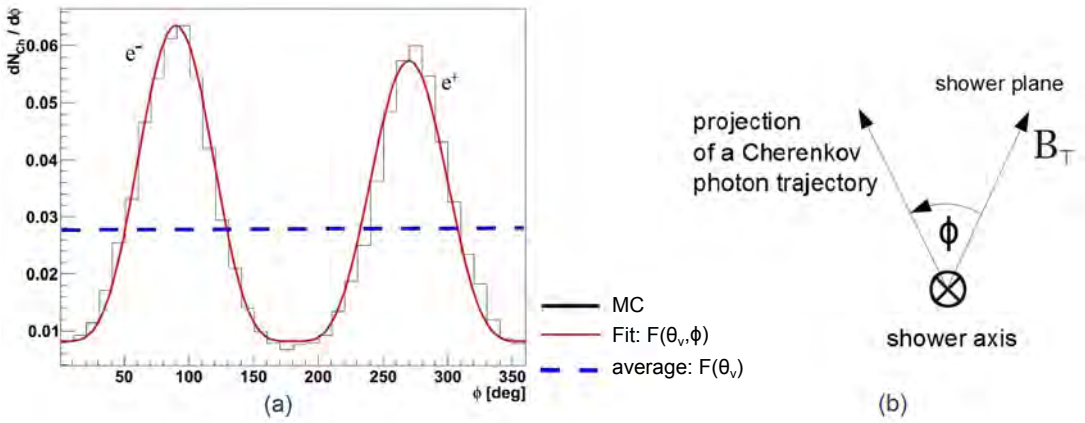

Figure 23: (a) Angular dependence of Cherenkov light with (red) and without (blue dashed) the ϕ parametrization for an iron primary with E=10^{17} eV, an zenith angle of 63° with B_T = 0.53 G and 10°<θ_v<12°. (b) Depiction of ϕ, the angle between the projections of the magnetic field vector and the viewing vector onto the shower plane perpendicular to the shower axis (from [64]).

shown example is an extreme one with a very strong magnetic field component $B_T = 0.53$ G, while the maximum field strength at the Pierre Auger Observatory site is around 0.3 G. Another restriction on the parametrization is that the viewing angle has to be between $2°-20°$. For larger viewing angles the intensity of direct Cherenkov light is dominated by the scattered fractions. Furthermore, the lack of Cherenkov photons in general outside this range limits the statistics. Thus the parametrization can not be applied to the LongXmax set, since for this events with $\theta_{\mathrm{vm}}<20°$ are rejected. Nevertheless, using the set with 4000 stereo events, the Cherenkov asymmetry was searched for in the data (as shown in the following). Since the magnetic field is weaker at the Pierre Auger Observatory, a less pronounced asymmetry than in Fig. 23a is expected.

6.3 Discrepancies in stereo events

To quantize the differences in the reconstructed energies of two eyes, a *pull* variable is defined as

$$\mathrm{pull} = \frac{E_2 - E_1}{\sqrt{\sigma_{E_1}^2 + \sigma_{E_2}^2}}$$

with the energies E_1 and E_2 of eye 1 and 2 respectively. By having the uncertainties of the energy in the denominator the pull is given in units of standard deviations. This way an easy description of any discrepancies is possible.
Since Cherenkov light is suspected to influence the energy reconstruction dependence on ϕ there has to be some way to test this. That's why an eye order is introduced in a way that

$$\text{Cherenkov fraction (Eye2)} > \text{Cherenkov fraction (Eye1)}.$$

This means in the pull the energy of the Cherenkov-poor eye is substracted from the energy of the Cherenkov-rich one. Moreover, the used ϕ for the plot is set to be the angle of the second eye[2].
The most common way to depict a changing dependence on a parameter is normal binning. However, in this work mainly a moving average is used, a method which is usually applied for time depending parameters. This means all points in a chosen window size are averaged, resulting in a smoother plot. On the one hand hidden trends are easier detectable, i.e. effects which are smaller than the

[2]Since ϕ is depending on the eye geometry, stereo events have two different ϕ angles, one for each eye.

fluctuations of the data. On the other hand it is especially beneficial when using small sets like the LongXmax stereo set (181 events). With simple binning each bin would contain only a very limited number of events, a problem which is avoided with the moving average. Moreover, looking at independent bins (without touching bars in x-direction) corresponds to the standard binning approach which means that using the moving average unites both ways of plotting data points. To demonstrate that both approaches are justified, in the later Sec. 7.1 simple binning is used.

To study the impact of the Cherenkov asymmetry correction on the set of 4000 stereos a θ_{vm}<20° cut has to be applied since the parametrization is only viable in this range. The pull is plotted against ϕ_2 in Fig. 24a. Before using the correction the shape resembles Fig. 23a: two peaks at similar angles (90° and 270°) with the second one having a smaller amplitude than the first. Interestingly, the resemblance to Fig. 23a might suggest that the shape is related to the displacement of electrons. However, the amplitude of the second peak is even more reduced than it is expected from the parametrization. The graph is not symmetrical around zero but shifted to more positive values. Surprisingly applying the correction hardly flattens the graph as the amplitude of the total effect is far larger than the correction. Apparently the shape has to have another origin and the Cherenkov asymmetry is just amplifying the effect.

A moving average with relatively large windows of 80° had to be chosen, as there are only very few events between 160°−200° in Fig. 24a. When choosing an ap-

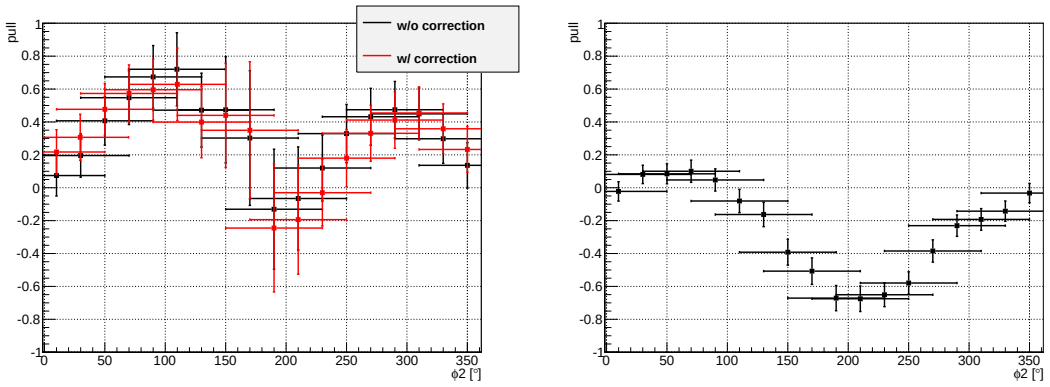

(a) **(b)**

Figure 24: Pull vs. ϕ for the 4000 stereo events set with (a) $\theta_{\mathrm{vm2}} < 20°$ and the Cherenkov asymmetry correction switched on (red)/off (black) and (b) $\theta_{\mathrm{vm2}} > 20°$.

propriate window width one has to make sure that the statistical uncertainty is not larger than the effect which can happen for too few events. The reason for the lack of events in this angular range is that with the $\theta_{\mathrm{vm}} < 20°$ cut mainly inclined showers can be detected (see Fig. 20a). This way, due to the orientation of the affected eyes (LL and LM) the viewing vector of these events is almost parallel to the B-field vector, resulting in a ϕ angle distribution centered around 0°. Moreover, the window size of 80° was selected since the trend is best visible this way. This is meaningful, as the feature is not narrow but has the scale of a few tens of degrees.

It should be recalled that events with the $\theta_{\mathrm{vm}}<20°$ cut are usually rejected because they complicate the correct calculation of the shower maximum, X_{max}, and lower the reliability of the data as explained in Sec. 6.1. For this reason the data with $\theta_{\mathrm{vm}}>20°$ is shown in Fig. 24b. The peaks are slightly shifted and also less pronounced, possibly due to the fact that events with large minimum viewing angles have smaller Cherenkov fractions. Moreover, the data points are even less symmetrical to zero, but this time shifted to negative values with a minimum at -0.75. Both peaks are not that visible and thus the graph can also be interpreted as one dip around ϕ =210°. So far the feature was only seen in the set with 4000 stereo events. Finding similar discrepancies in official high quality sets would indicate the importance of this effect.

As can be seen in Fig. 25, the data points based on the stereo LongXmax data set are less sine-like but instead rather close to zero for half of the ϕ range. Between $180°-270°$ however (and thus mainly in the ambit of LM) a clear feature appears, showing a negative pull exceeding -1 and thus being even more significant than in Fig. 24b. Obviously in this ϕ range larger discrepancies between the two reconstructed energies occur. The existence of the feature in an official set justifies using the 4000 stereo set as apparently the lack of cuts in the latter isn't the cause of the discrepancy. This significant dependence in the LongXmax stereo set is not seen when using a random eye order, i.e. without stressing the Cherenkov light influence. With the definition of the eye ordering in mind, this means that for some reason in the range $180°-270°$ Cherenkov-rich energies are underreconstructed or Cherenkov-poor ones are overreconstructed. Apparently the data is sensitive to ϕ, which is by definition related to the eye geometry w.r.t. the magnetic field of the Earth.

When comparing the data with simulation (also Fig. 25) several things attract attention. Not only are the data points near zero and thus both eyes have very

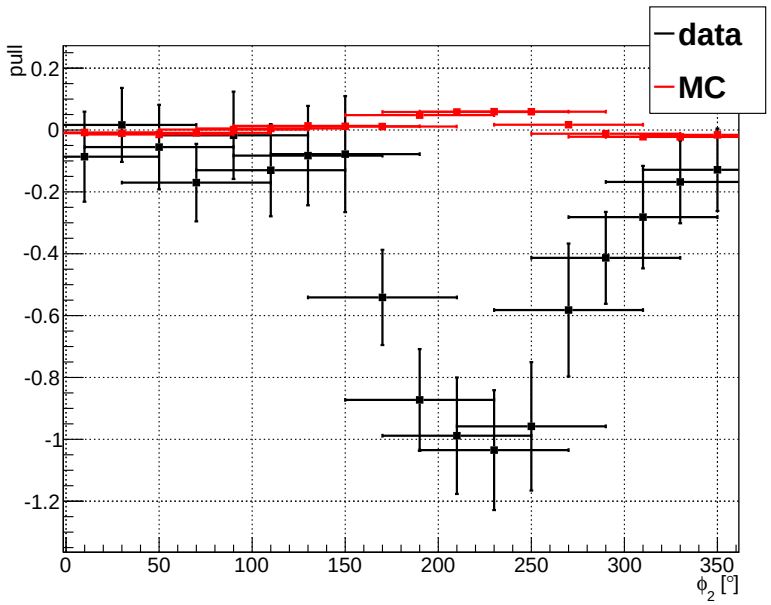

Figure 25: Pull vs. ϕ for the stereo LongXmax set with ordered eyes. For the data a feature is revealed around $\phi = 230°$ while the simulation shows almost no angular dependence.

similar reconstructed energies, but there is almost no angular dependence. In the feature range of the data however, small differences can be found which result in a slightly positive pull, contrarily to the negative values seen in the data. This could be due to a Cherenkov reconstruction bias which is introduced later. In general, we observe a nearly perfect flatness in MC which is understood, unlike the shape seen in the data. This disagreement in flatness to the data is striking and should have its origin in one of the differences between the two sets. Possible explanations could be the handling of the aerosols or the spot halo which are both not simulated. Since for the MC reconstruction all calculations are based on the longitudinal profile, dependencies on the lateral profile (for example of the B field) are hidden or not present at all. Finally, as it is the nature of simulations, only known effects are taken into account so if there are processes in reality which were not studied yet completely (e.g. the influence of the sun activity), they are not simulated. Since the eye order indicates that the feature might be connected to Cherenkov light, any differences in the reconstruction of this component are expected to change the behaviour of the pull.

What could cause these discrepancies between reconstructed energies of various eyes? Possible explanations range from additional light from unaccounted physics effects (see for example section 3.5), miscalibration of the eyes to misreconstruc-

tion of the detected light. At this point, errors in the reconstruction algorithms are considered unlikely because in this case the simulated data shouldn't be flat in ϕ like it is seen in Fig. 25. To strengthen the statement that discrepancies in energy reconstruction exist one can look into the golden hybrid data set to perform additional reasonable cross-checks.

6.4 Further cross-checks

Does the feature disappear for specific data sets or parameter ranges? To answer this question, it has to be studied under different conditions. The most meaningful cross-checks are shown in the following.

6.4.1 The ϕ dependence in hybrid events

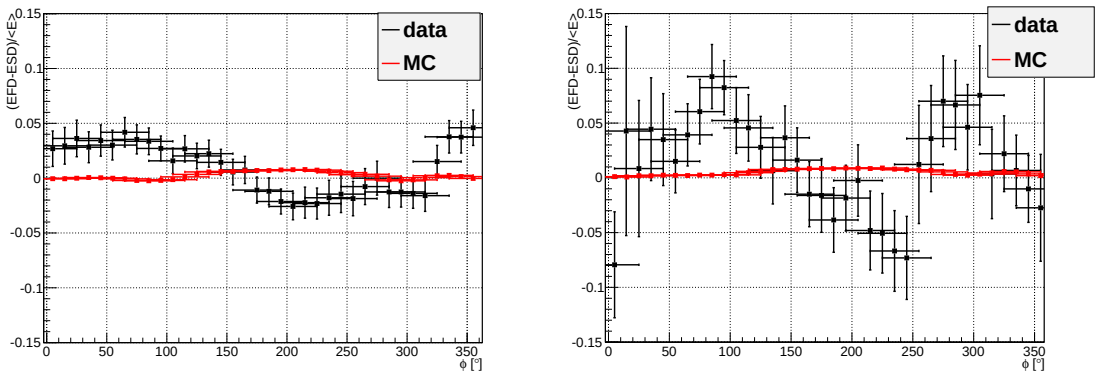

Figure 26: Relative energy vs. ϕ of the corresponding FD using the golden hybrid set and Naples MC with (a) the golden cuts and (b) additional $\log(E_{\mathrm{SD}}/\mathrm{eV})>19.2$. MC events are shifted around zero by scaling E_{SD} with 1.25.

First the energy differences are checked for the golden hybrid set. If the feature has an effect only in stereo events, comparing E_{FD} and E_{SD}, the reconstructed energies of the FD and SD, should show no significant difference. Both detection techniques have different energy uncertainties which would introduce a bias when using the pull variable. Instead of the pull one should use the relative energy difference

$$\frac{E_{\mathrm{FD}} - E_{\mathrm{SD}}}{\langle E \rangle},$$

which doesn't rely on energy scale uncertainties. Since only one eye is used, any ordering is omitted. Moreover, when looking at simulated SD energies, a scaling has to be applied because E_{SD} is systematically underreconstructed as explained in Sec. 6.1.1. Despite the known shift, which does not depend on ϕ, conclusions can be made about the angular dependence on ϕ.
In Fig. 26a the relative energy difference of the golden hybrid set is plotted against ϕ of the used FD eye. A feature is visible in the data with relative energy differences of up to 8% between minimum and maximum. As a comparison, the maximal pull value from the stereo events corresponds to -11% relative difference and thus an even stronger discrepancy. For high-energy events ($\log(E_{\mathrm{SD}}/\mathrm{eV})>19.2$) the feature is much more pronounced, though (Fig. 26b) and has a different shape. Relative differences of 18% in total are reached and the plot shows some resemblance to the set with 4000 stereo events (Fig. 24a): two peaks with the one at 300° slightly smaller. The simulation shows the same behavior in both plots, no discrepancies occur which results in a flat distribution around zero, similar to the stereo events. Another intriguing characteristic of the feature would be a possible energy dependence which will be later shown in Sec. 7.1.1.

6.4.2 Relative energy differences between separate FD stations

Ideally all FD station work under the same conditions. In reality, this is not possible and there are small differences between them which can influence the measurement like the varying dust coverage of the windows at the FD station which are transmitted by the light or the different orientation of each building. Is the observed discrepancy in energy reconstruction based on these differences between the eyes? When plotting the relative energy against E_{FD} for each eye separately, some dependences appear in the data (Fig. 27a): LL, LM and LA show only a small shift, CO however has an inverted shape and seems to measure energies that are always higher than the corresponding SD energy. While the former three FD stations have a similar elevation between $1400-1416$ m, CO is about 300 m higher. This way not only higher energies can be detected, the light reaching CO might be attenuated less due to less aerosols locally in front of CO. Aerosols as possible explanation are supported by the MC (Fig. 27b), since they are not considered in the available simulation. The different eyes are practically indistinguishable, there is no actual order in energy since all eyes observe the same energies, only LA reconstructs slightly lower energies than the other eyes.

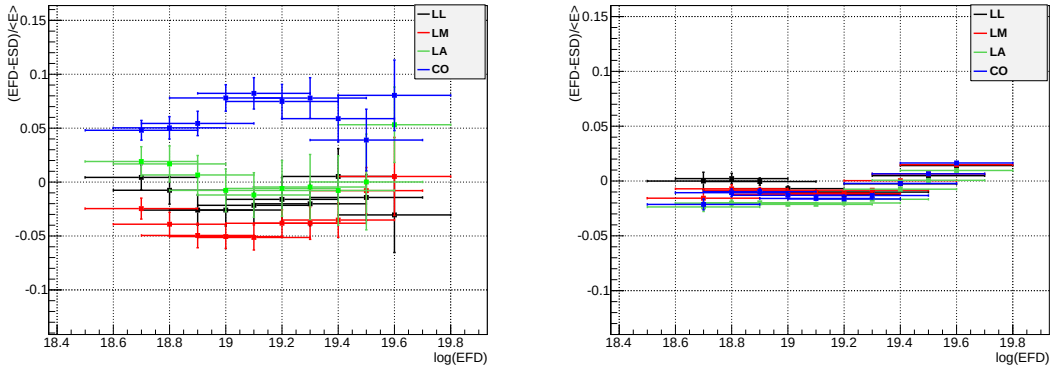

(a) (b)

Figure 27: Relative energy vs. E_{FD} for each separate eye based on (a) the golden hybrid set and (b) the MC from Naples. MC events are shifted around zero by appropriate scaling of E_{SD} with 1.25.

Moreover, for high energies the same weak trend in energy is visible for each eye, contrary to the data in which CO shows a different trend in comparison to the other eyes at the whole spectrum. Again E_{SD} was scaled to shift the graph around zero.

To show that the observed differences are mainly caused by the eyes and not simply by the varying ϕ range, these two cases are compared for the most extreme eyes, CO and LM. In Fig. 28a all events in two distinct ranges ($0°<\phi<100°$ and $200°<\phi<300°$) are considered and relative differences of 5% are visible. When adding the appropriate eye requirement (i.e. for example that events with

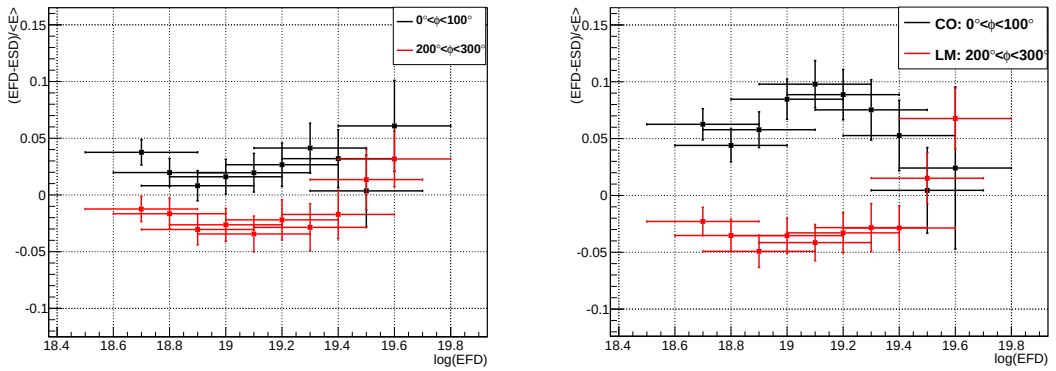

(a) (b)

Figure 28: Comparison of the influence of the eyes and the ϕ range in the energy differences. (a) Simple cut on the ϕ range and (b) with an additional eye cut.

$0°<\phi<100°$ have to be observed in CO) the gap increases to 8−13% (Fig. 28b). Thus the origin of the measured discrepancies rather lies in the eyes than in the ϕ range. Differences in the energy reconstruction between the eyes might suggest a miscalibration and are studied more closely in Sec. 7.1.
An alternative explanation for these differences could be the different observed sky regions. There are theories which introduce a dependence of the air shower on the sky region it's arriving from (e.g. preshower-induced showers in the radiation belts around Earth).

6.4.2.1 Removing the CO eye

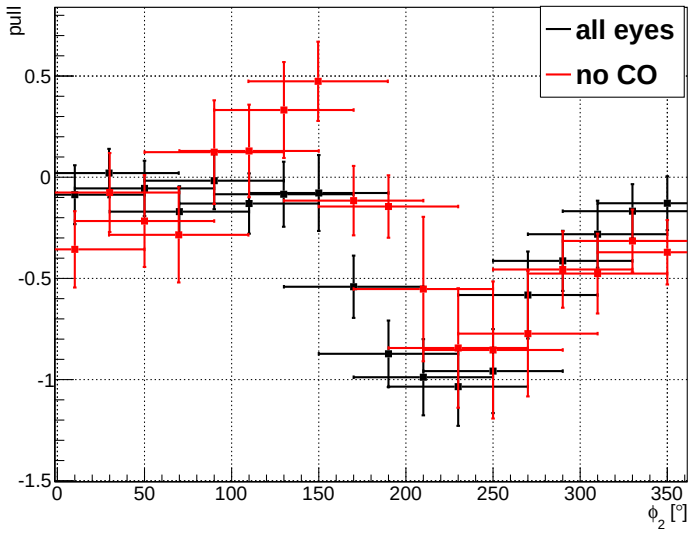

Figure 29: Feature plot for the stereo LongXmax set with all eyes and without CO. For both cases, significant discrepancies are visible.

Since in Fig. 27a the CO curve shows the largest discrepancies to the other eyes one might assume that CO is also responsible for the feature. Thus the feature plot is repeated in Fig. 29 but now only stereo events without CO are considered which decreases the statistics down to 71 events. As a comparison the previous seen plot with all eyes is included. Despite the low statistics the feature is clearly visible again, although the dip is slightly less pronounced and a small additional peak appears around 150°. Obviously the difference between CO and the other eyes can not be the only cause of the feature and a more complex origin than a pure miscalibration is indicated. Also removing one of the other eyes doesn't let the feature disappear.

6.4.3 Dependence on the magnetic field

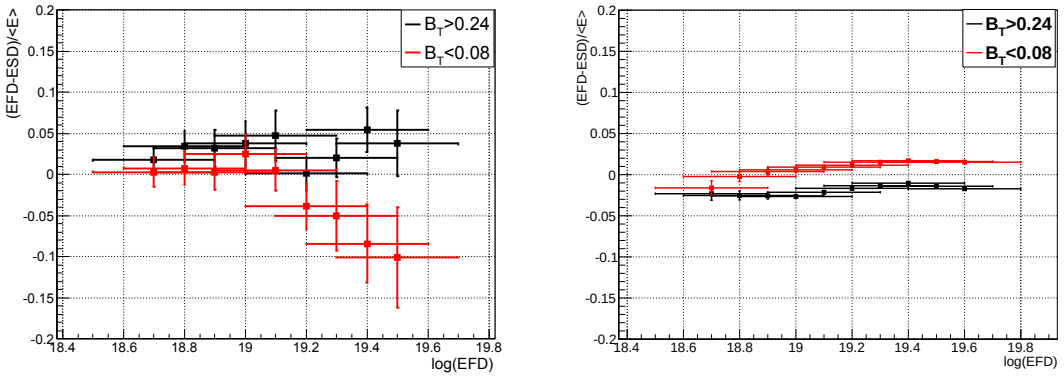

Figure 30: Relative energy vs. E_{FD} with cut on the geomagnetic field based on (a) the golden hybrid set and (b) the MC from Naples. MC events are shifted around zero by appropriate scaling of E_{SD}.

The pull (and the relative energy difference) is depending on ϕ which depends on the transversal magnetic field component, B_T, so it is logical to look at the feature for weak and strong B_T. A cut was applied in Fig. 30a and data events with weak (<0.08 G) and strong (>0.24 G) B_T are shown. Surprisingly events with a strong field are rather unaffected and show no differences between the reconstructed energies. In agreement with Fig. 26b this doesn't hold for high energy events ($\log(E_{\mathrm{FD}}/\mathrm{eV}) \geq 19.2$) with a weak field which show a relative energy difference of 10%, i.e. the effect seems to be suppressed by the magnetic field. In Sec. 7.4 this is further discussed. The MC set with golden cuts applied shows again a flat distribution for both graphs around zero but with a small gap of 3% difference. As shown in Ref. [65], the SD energy estimator is influenced by a geomagnetic effect. Therefore, the SD energy is over/underreconstructed depending on the arrival direction. This effect has to be taken into account for the E_{SD} reconstruction but currently it is not yet included in the reconstruction chain and thus a probable cause for the small gap. Moreover, the sign of each data selection is reversed: events with small B_T reconstruct larger energies in FD than events with a strong field.

7 Possible explanations of the Features

After in Sec. 6 the existence of the features was introduced and confirmed by various cross-checks, the question is what is causing the observed discrepancies. Therefore different ideas and approaches are discussed in the next chapter.

7.1 Miscalibration

Based on the findings in Sec. 6.4 the different energy calibrations of the various eyes could be a reason for the observed features. A possible miscalibration was studied by assigning an energy coefficient c_i to each eye i, covering the range between $0.9 - 1.1$ in steps of 0.02. All of the $11^4 = 14641$ configurations were tested by determining the flatness of the golden hybrid data points with a χ^2 fit. Figure 31 shows a comparison of the feature with and without the coefficients which flatten the feature. The reduced χ^2 decreases from 8.1 (before recalibration) to $\approx$1. This was done with the coefficients $c_{\mathrm{LL}} = c_{\mathrm{LM}} = 1.04$, $c_{\mathrm{LA}} = 1.00$ and $c_{\mathrm{CO}} = 0.94$ which indicates that energies in CO are overreconstructed and energies in LL and LM are underreconstructed as already seen in Fig. 27a. Using these factors flattens the feature to only 3% difference at maximum and

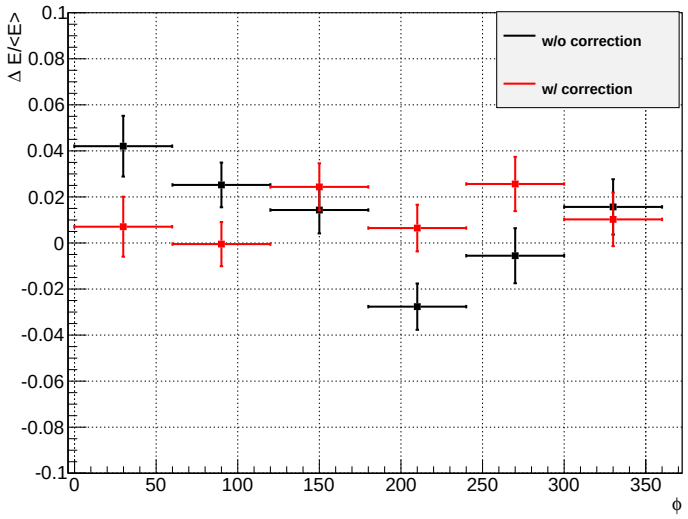

Figure 31: Comparison of the feature in the golden hybrid set before and after using the coefficients $c_{\mathrm{LL}} = c_{\mathrm{LM}} = 1.04$, $c_{\mathrm{LA}} = 1.00$ and $c_{\mathrm{CO}} = 0.94$ to flatten the graph as good as possible.

thus a small miscalibration is suggested. To check these values one can look at the relative energy difference of stereo LongXmax events and study all possible eye combinations. An additional cross-check can be used since the calibration was also examined in Ref. [51]. To compare the recalibration values with the relative energy differences, the ten recalibration configurations with the reduced χ^2 closest to one were normalized to one of the appropriate eyes. The average for each eye combination can be found in Tab. 1 with the data from the stereo set and the values from [51]. The measurements are in very good agreement within the uncertainties and almost all of the values are in the uncertainty interval. Usually this would imply an overestimation of the uncertainty, but since only the statistical one was used, this can't be the case here. Although different sets were used (golden hybrid vs. stereo) the best agreement is between the recalibration factors and the values from [51].

Eyes	recalibration	stereo set	Ref. [51]
CO-LM	1.08±0.01	1.09±0.03	1.07±0.02
LL-CO	0.93±0.01	0.91±0.02	0.90±0.01
LM-LL	0.99±0.01	0.97±0.02	0.98±0.01
LA-LM	1.04±0.01	1.03±0.03	1.06±0.02
CO-LA	1.04±0.02	1.01±0.02	1.04±0.01

Table 1: Shown are the relative energy differences calculated by the recalibration coefficients, found in the stereo set and in [51] respectively for each pair of eyes. The pair LA-LL is missing due to low statistics.

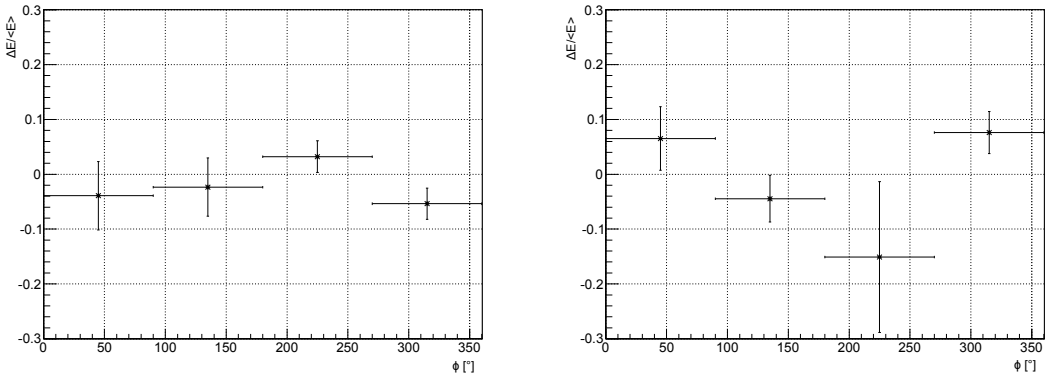

(a) **(b)**

Figure 32: Different shapes in relative energy difference for mean viewing angles between (a) 65°−75° and (b) 75°−85°.

If the feature is really explained by a miscalibration it should be independent of the mean viewing angle (viewing angle at the center of the FOV). As can be seen in Fig. 32 this doesn't seem to be the case. The shape strongly differs between two arbitrarily chosen mean viewing angle intervals, $65°-75°$ and $75°-85°$. While the former is rather flat (red. $\chi^2 = 1.4$) the latter shows relative differences of more than 20% in total (red. $\chi^2 = 13.9$). A flatness test was performed against the mean viewing angle for events at LM as an example. For each bin in Fig. 33 the χ^2 of all contained events was determined, the plotted value is $\log(p)$. The p-value

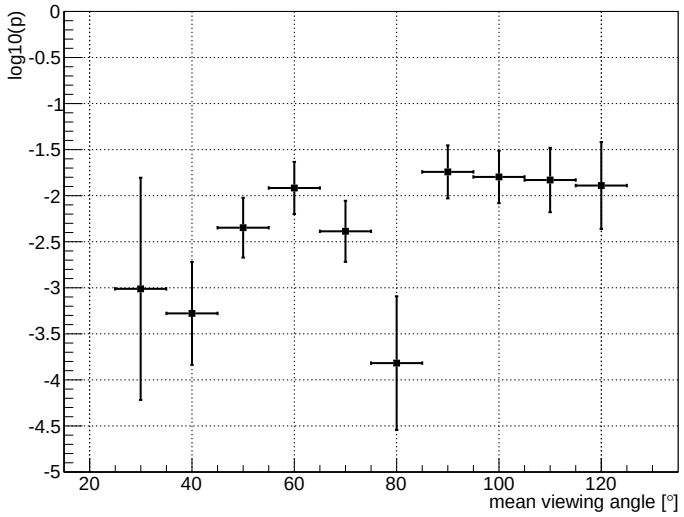

Figure 33: Flatness test of relative energy difference of LM events in relation to the mean viewing angle.

denotes the probability that the observed χ^2 exceeds the value χ^2 characterizing the obtained goodness of fit by chance, even for a correct model. The more negative the value in the plot, the lower the probability. Each bin contains 50 events since bins with an uniform width and the same number of events are needed to prevent biases. The number of events per bin were chosen due to the number of available events in the bins with smaller viewing angles. With these 50 events a curve was calculated like in Fig. 32 and the resulting p-value was used. Between the range $20°-100°$ in mean viewing angle one can see variations in the data with p-values between 0.0002 and 0.02 which are difficult to explain by a pure miscalibration.

Thus, a dependence on the viewing angle is indicated by the data, but to be more convincing a further analysis with larger statistics is required.

7.1.1 Eye-to-eye differences

When studying again stereo events of the LongXmax set with the introduced Cherenkov fraction eye order, one can look at events with specific eye combinations like CO/LL and LA/LM and plot the pull with $E_{\mathrm{CO}} - E_{\mathrm{LL}}$ and $E_{\mathrm{LA}} - E_{\mathrm{LM}}$ respectively against E_{CO} or E_{LA}. Moreover, one differentiates between which FD station is eye 2 (see Fig. 34).

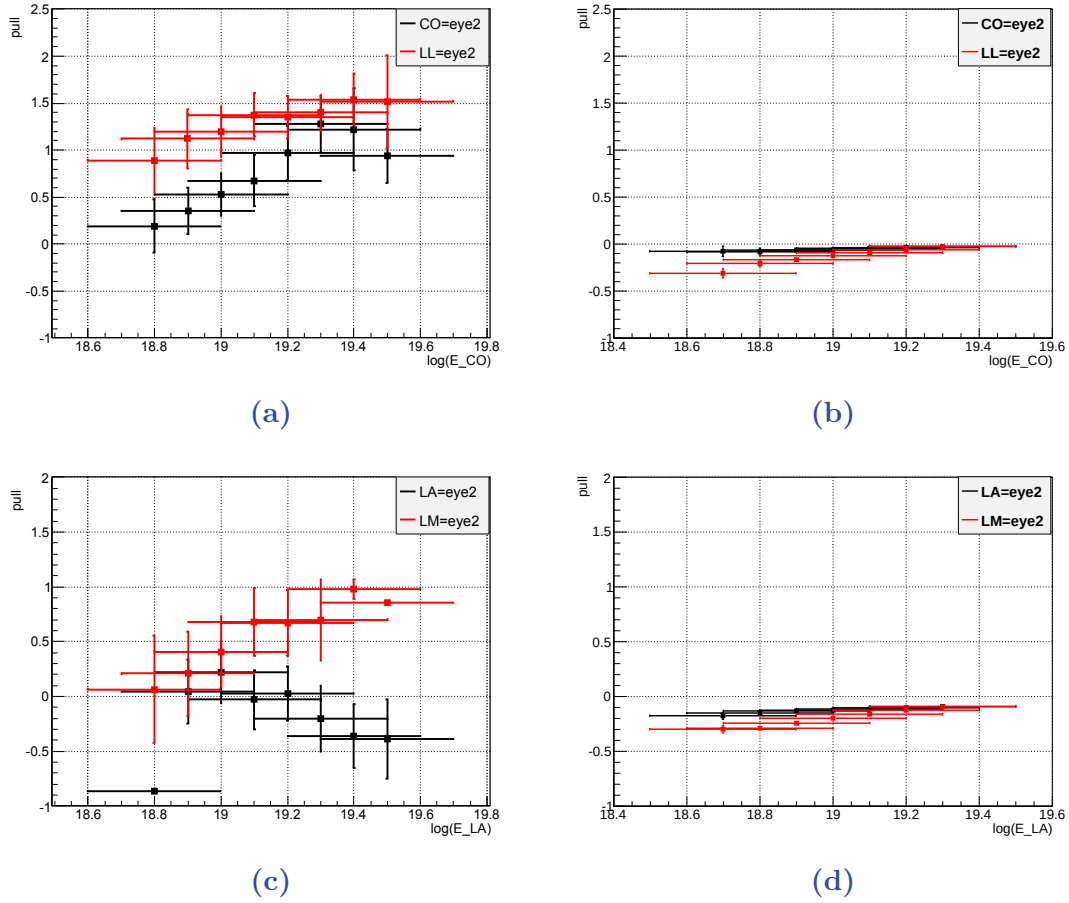

Figure 34: Eye-to-eye differences for stereo events of the LongXmax set with specific eye pairs. Now the energy difference in the numerator of the pull is fixed as $E_{\mathrm{CO}} - E_{\mathrm{LL}}$ in (a) data and (b) MC as well as $E_{\mathrm{LA}} - E_{\mathrm{LM}}$ in (c) data and (d) MC. As a reminder, eye 1 is defined as being Cherenkov-poor and eye 2 as being Cherenkov-rich.

The CO/LL pairs (Fig. 34a) have a trend in E with the largest pull for the highest energies. Since all values are positive, E_{CO} has to be larger than E_{LL} in all cases which agrees to all previous considerations (Fig. 27a as well as the obtained calibration factors and the seen relative energy difference of 10% for

CO/LL from Sec. 7.1). Additionally, a gap between CO and LL as eye 2 is clearly visible, showing the largest discrepancy from zero when CO is a Cherenkov-poor event and thus pointing to the importance of the Cherenkov reconstruction. The simulation (Fig. 34b) is flat as expected, but also showing a very small gap for low energies and thus a little impact of the Cherenkov light even for simulations. This is a known bias and will be shown later. Moreover, like in the magnetic field plot (Fig. 30b) the order of the graphs is reversed.
Stereo events measured in LA/LM (Fig. 34c) show a similar gap as in the other pair of eyes but within an opposite energy trend for LA as eye 2. The data points in this case are mostly negative, contrarily to LM as eye 2 which means that the energy of the Cherenkov-poor eye is larger than the energy of the Cherenkov-rich one. This might imply that Cherenkov light is underreconstructed. The MC plot (Fig. 34d) is very similar to Fig. 34b and shows a small shift towards the negative which is caused by the observed weak eye order that showed that LA observes the lowest energies.
LA and LM have almost the same elevation, so still observing differences is an argument against the influence of aerosols only due to different elevations.
Since neither the energy nor the viewing angle dependence can be explained by the miscalibration, it is rejected as only reason for the seen peculiarities. Nevertheless, the differences between the energy reconstruction for each eye seem to contribute to the features.

7.2 Re-reconstruction and VAOD issues

The eye-to-eye differences in Fig. 34a were produced using the LongXmax data, the current official data set. How does the plot look like with the older ICRC11[3] set from 2011 and the corresponding reconstruction algorithms? This is depicted in Fig. 35a. Surprisingly both the energy trend and the influence of Cherenkov light are almost completely gone. The reason for this has to be either the differences between the used events in each set or the improved reconstruction algorithms. The old Offline version v2r7p2 didn't consider the aforementioned halo correction (although already implemented) and had to use an older VAOD database. Especially the latter can have a huge impact on the energy reconstruction and thus has to be measured precisely. To check these three options,

[3]The set on which the $X_{\max}$ publications of the International Cosmic Ray Conference in 2011 are based on [66].

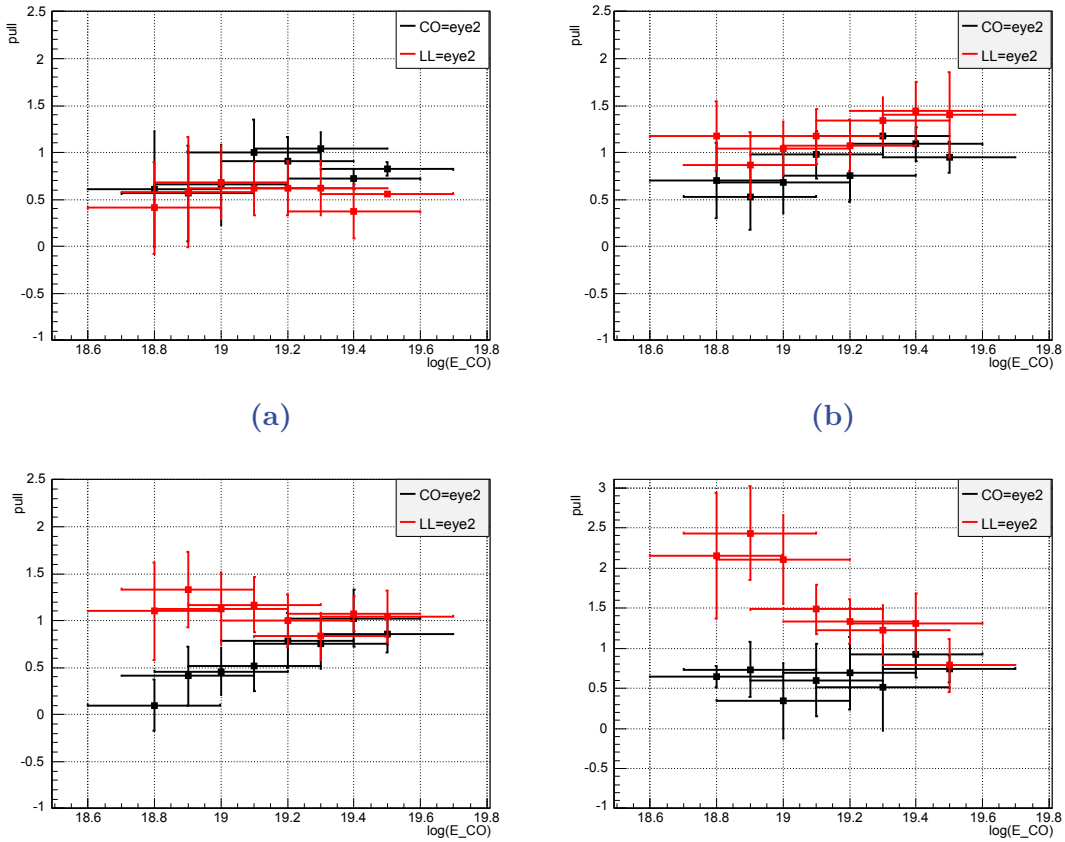

Figure 35: (a) Eye-to-eye differences for CO/LL stereo events using an old reconstruction with the ICRC11 set (Offline version v2r7p2). Re-reconstruction with the LongXmax set and the current Offline version v3r0p0 but (b) no halo, (c) using the old VAOD database or (d) with the events of the ICRC11 set, are shown.

re-reconstructions were performed with the current Offline version v3r0p0. In Fig. 35b the halo correction was switched off, Fig. 35c relies on the old database and in Fig. 35d the same events are used as in the ICRC11 set. While none of the plots solves the problem, the one with the old halo setting at least decreases the gap and might indicate some connection to the feature. Although, when using the older, misreconstructed Naples MC set where the halo treatment was incorrectly included, the feature also didn't appear which weakens this hypothesis. The data points in all plots are positive and thus always $E_{CO} > E_{LL}$ in agreement with previous plots.

Using another VAOD database also decreases the gap at least for high energies and remains a big error source as shown in Fig. 36. The $\mathrm{d}E/\mathrm{d}X(X)$ profile is

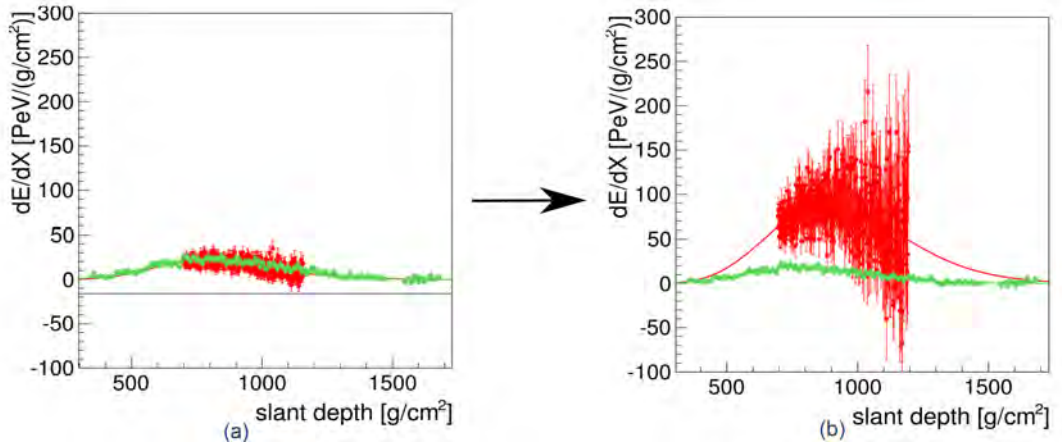

Figure 36: Reconstruction of the stereo event with ID 201004704450 using an (a) old and (b) updated atmospheric database. The event was observed by the eyes CO (green) and LA (red).

shown for a stereo event. While the reconstructed energies match very well for the older Offline version v2r7p8 with an old VAOD database, for the newer one a huge discrepancy appears, resulting in a large pull. This is due to the fact, that the old version didn't include any aerosol measurements to this eye and used the values from the next available FD station. After an update the atmospheric data was analyzed and a large aerosol value was assigned to this event which

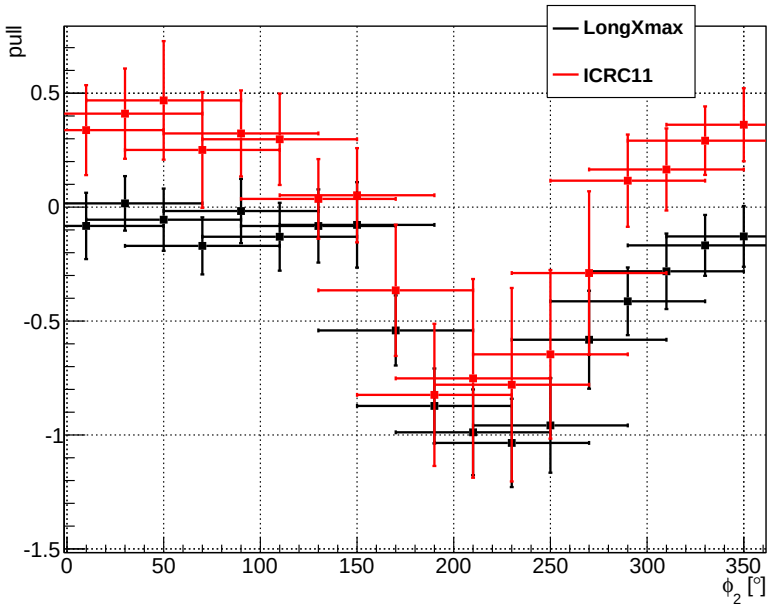

Figure 37: Pull vs. ϕ_2 with eye ordering for stereo events of the ICRC11 set in comparison with the already studied LongXmax data.

was rejected consequently. Clearly, the lack of VAOD values or using incorrect ones makes a huge difference and thus this potential source of uncertainty has to be treated carefully. This work led to the discovery of incorrect values in the atmospheric analysis which might indicate some laser calibration issues. Since the quality control for this analysis seems to be currently insufficient it should be improved and appropriate studies are ongoing.
When plotting the original feature for all ICRC11 stereo events (Fig. 37) it becomes evident that the discrepancies didn't vanish at all. Thus the changes between the sets rather affect the energy dependence and impact of Cherenkov light as was seen in the flatter distribution with decreased gap in Fig. 35a, and not the ϕ dependence. Apparently we see an interplay of various features, different things seem to be responsible for the energy discrepancies, the energy trend and the Cherenkov light influence.

7.3 Reconstruction of Cherenkov light

Due to the results of Sec. 6.3 and 7.1.1 a possible misreconstruction of Cherenkov light in the LongXmax data is studied. In Fig. 38 the quality of the energy recon-

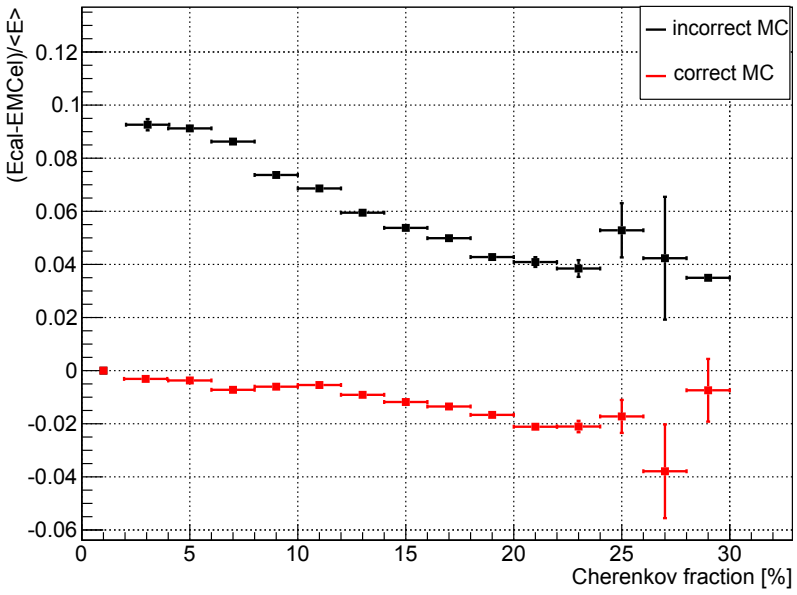

Figure 38: Cherenkov reconstruction quality of the old and new Naples MC set with LongXmax cuts. Compared are the electromagnetic and calorimetric energies E_{MCel} and E_{cal}.

struction algorithms for different Cherenkov fractions is demonstrated for the old MC set with the halo setting issues and the improved one which was eventually used for the thesis. When using the electromagnetic and calorimetric energies E_{MCel} and E_{cal} (see Sec. 5.3) one avoids considering the invisible energy which is not known and has to be parametrized. This plot significantly contributed to finding the halo issue and thus improving the quality of the set for the whole Auger community. As can be seen, the relative differences reached 9% for the old set while for the new one 2% are basically not exceeded. Although the energy reconstruction is still not perfect, after using the improved MC the bias is acceptable. Moreover, the observed bias is too small to explain the peculiarities seen in the data, hence the Cherenkov reconstruction is not the reason for discrepancies of 10%.

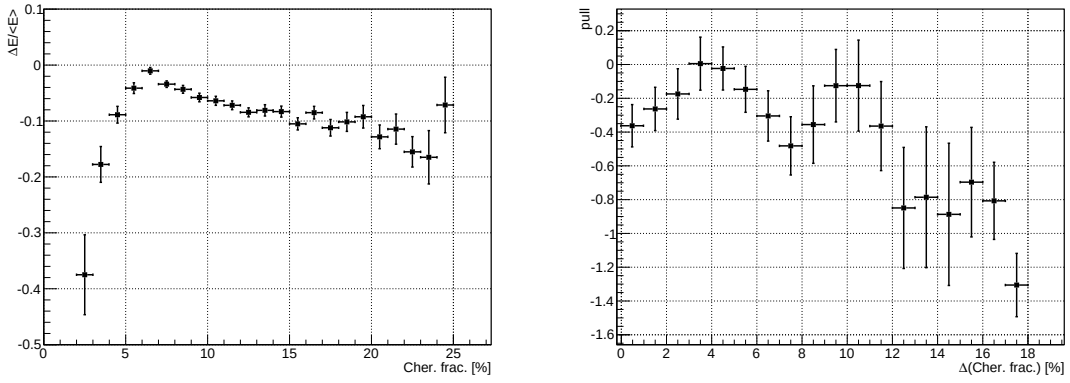

(a) **(b)**

Figure 39: (a) Relative energy difference of hybrid events with $E_{\mathrm{FD}} - E_{\mathrm{SD}}$ against Cherenkov fraction for the LongXmax set. Due to the θ_{vm}<20° cut the observed Cherenkov fractions stop around 25%. In (b) the pull of stereo events were used, which provide two different Cherenkov fractions, hence the difference of them is shown. Once again, the pull is defined with the Cherenkov-dependent eye order.

Now the dependence of the discrepancies on the Cherenkov fraction for the hybrid data set is shown in Fig. 39a. Events with Cherenkov fractions around 7% (which are the most common, see Fig. 40) have only small differences in energy, whereas events with rarer fractions (closer to zero or above 15%) show larger deviations. For stereo events something similar can be seen: the larger the difference of detected Cherenkov light in the eyes, the more probable is the presence of rarer fractions and a large disagreement in the reconstructed energy is observed. An underreconstruction of energy from Cherenkov light would show the same behaviour, the more Cherenkov pho-

tons are involved, the more different would both energy reconstructions be. Just the events with lowest Cherenkov fractions in Fig. 39a seem to disagree with this hypothesis, since one would expect no differences for these; although there are only very few events in this range. Moreover, once again due to the usual eye order, all values being negative alludes to an underreconstruction of energy coming from Cherenkov light. At this point it is not known yet, if this is a result of a misreconstruction or rather the manifestation of a physical effect.

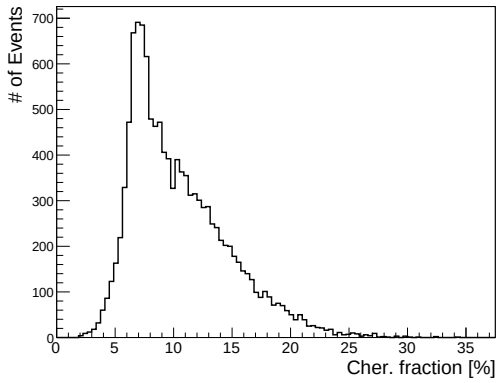

Figure 40: Distribution of the Cherenkov fraction for the hybrid LongXmax set.

How does the Cherenkov fraction varies with ϕ? This is shown in Fig. 41 for the complete LongXmax set and the Naples shower with appropriate cuts. In the middle there is a dip for both data and simulation. The observed structures could be influenced by the backwall angles of the FD stations. Since the layout is not symmetrical w.r.t. the magnetic field vector one would not expect a flat distribution in ϕ. The most striking finding is the discrepancy in Cherenkov fraction for the data and MC. The latter observes

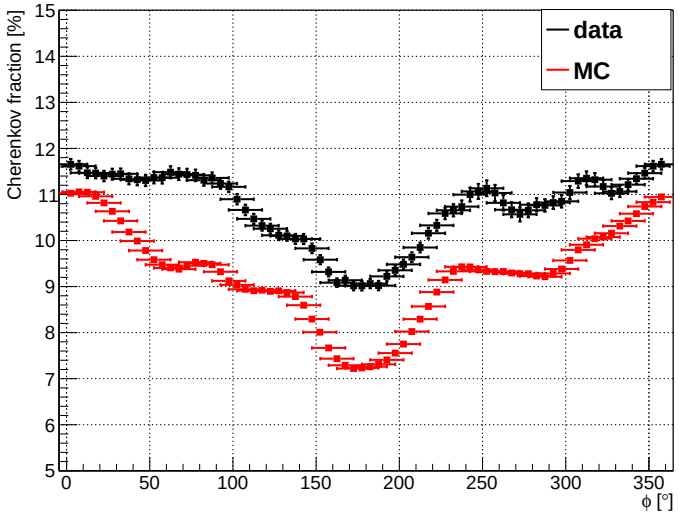

Figure 41: Cherenkov fraction dependence on ϕ for the LongXmax set and the corresponding simulations.

Cherenkov fractions which are 1−2% smaller than in the data for the complete ϕ range. While this could be explained theoretically by different energy distributions in the sets, the earlier seen dependence between the minimum viewing angle and the measured Cherenkov fraction in Fig. 20b contradicts this hypothesis. Although in this plot the geometries are the same for both sets the discrepancies appear and in the data there is more Cherenkov light reconstructed. Further studies are recommended to explain this difference.
It follows that the number of Cherenkov photons is overreconstructed in the data, while the energy coming from Cherenkov light is simultaneously underreconstructed, as seen in the feature plots with stereo events.

7.4 Influence of the magnetic field

So far the energy discrepancies appeared in the plots either as dip around 200°−250° in ϕ (Fig. 24b and 25) or as two peaks with positive and negative pull values (Fig. 24a and 26b). Understanding the differences in shape could lead to an easier explanation of the features. The results of Sec. 6.4.3 and the

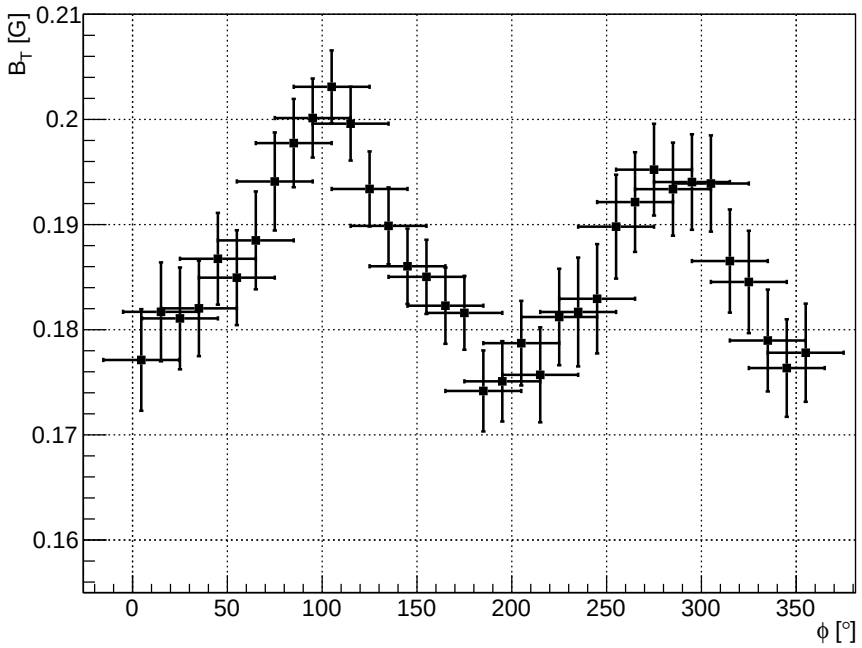

Figure 42: Distribution of B_T for the golden hybrid data set. Two peaks with different heights around 100° and 280° appear, similar to the feature plot for this set, Fig. 26b.

definition of ϕ motivate a deeper study of the influence of B_T on reconstructed energies. The projected field component is plotted against ϕ for the golden hybrid data set in Fig. 42. B_T varies from 0.18 to 0.20 G and two peaks are visible with different heights, similar to the corresponding feature plot (Fig. 26b) and the largest energy discrepancies are observed for the ϕ ranges with highest deviation from the average B_T.

To check whether this is a mere coincidence the other feature plots with different conditions can be compared with the B_T distribution. In Fig. 43a the magnetic field component of the large stereo set is plotted with the cut in θ_{vm} for comparison with 24. For large minimum viewing angles (θ_{vm}>20°) the similarities are evident again and the pull deviations appear in the ϕ range with the lowest B_T. Could the reconstruction algorithms be based on larger B_T and thus not valid for lower values? For θ_{vm}<20° however, this is no longer true: although the shape is sine-like for both plots, they are shifted to each other by 90° or alternatively the extrema are inverted and dips in Fig. 43a coincide with peaks in Fig. 24a. The weaker the magnetic field, the more the second peak in the latter plot is reduced which matches to the observation that this peak in the data is even more reduced than expected from the parametrization.

The other factor contributing to the different shapes is the energy of the event. The B_T distribution for the complete LongXmax set is shown in Fig. 43b with a cut at $\log(E/\mathrm{eV}) = 18.5$. While low-energy events have a reduced B_T between 100° and 300° (compare to the feature in Fig. 25), events with higher energies show the familiar distribution of two peaks with different heights (compare to

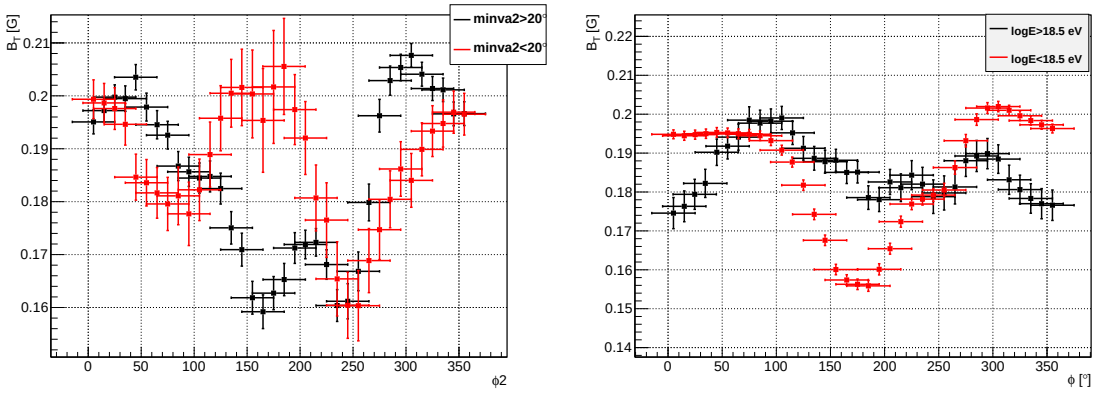

(a) (b)

Figure 43: (a) Distribution of B_T against ϕ_2 for the large stereo set and a cut in θ_{vm} and (b) against ϕ for the LongXmax set and a cut in energy.

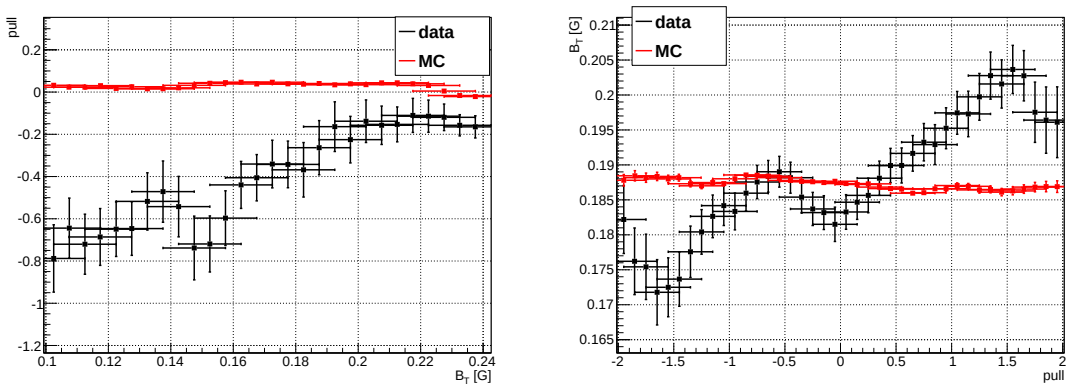

(a) **(b)**

Figure 44: (a) Pull vs. B_T and (b) B_T vs. pull for the large stereo set along with the corresponding MC. Only in the data a strong dependence can be seen.

the feature of the golden hybrid set in Fig. 26b which has only events that pass, among others, a $\log(E/\text{eV}) > 18.5$ energy cut).

Finally, when looking at the relation between the pull and B_T for the large stereo set, the impact of the magnetic field can be illustrated best. As shown in Fig. 44a, there is a strong dependence and for weak B_T, especially below 0.2 G, the energy differences between two eyes are the largest. Exchanging the variables on the axes doesn't necessarily return a consistent look (Fig. 44b): while negative pull values correlate again with weak magnetic field components, for positive values the opposite is true. When speaking in absolute numbers, most events are near zero pull or slightly negative with a strong B_T. Events with a positive pull are in the minority and mainly coming from the set with inclined showers ($\theta_{\text{vm}} < 20°$). Interestingly, for these events the strongest magnetic fields were observed. Apparently there is a class of events for which the energy reconstruction is sensitive to B_T. Moreover, there is no such development visible in the simulated set.

These similarities in corresponding plots show that the role of B_T in the explanation of the observed peculiarities is significant. In this case some unaccounted physical effect which causes the discrepancies would become more probable. The remaining mystery is the nature of this effect, which seems to be suppressed for strong magnetic fields.

8 Summary and Outlook

At the Pierre Auger Observatory, energies of air showers can be reconstructed in various ways. When comparing the reconstructed energies of two FD stations in stereo events as well as the energies observed in the SD and one FD station in hybrid events, significant discrepancies between them were found.
The characteristics of this feature were studied: a weak magnetic field and high energies seem to favor its appearance. By introducing an eye order in Cherenkov fraction for the stereo events the influence of Cherenkov light has been proven. Moreover, the feature is strongly depending on the angle ϕ. While for stereo events primarily events with $200°<\phi<250°$ are affected, hybrid events show differences in energy reconstruction for almost the whole angular range.
The reason for the observed discrepancies is not clarified yet, although various possible origins were studied. Differences between the individual FD stations seemed to indicate some miscalibration which was analysed by applying self-determined coefficients to the energies. This recalibration decreased the significance of the feature, but is still not sufficient to explain it. Furthermore, the aforementioned dependence of the feature on the energy as well as the viewing angle contradicts the miscalibration hypothesis as the sole reason for the differences in energy reconstruction. Moreover, since each eye is looking into different sky regions it should be studied how the arrival direction affects the feature.
While the data suggests an underreconstruction of energies from Cherenkov light, simulations show that the reconstruction algorithms could only explain deviations not larger than 2%. Moreover, since the features do not appear in any MC plots a misreconstruction as explanation becomes unlikely. Nonetheless, the different fractions of Cherenkov light in data and simulation have to be examined since this remains a potential source of error.
Finally, the rejections of other explanation and the severe influence of the magnetic field argue in favor of an unaccounted physical process as the origin of the features. As this effect would not be considered yet, it also wouldn't be simulated and thus the MC plots could be explained. The question remains which phyiscal effect would be responsible for this. An example was given which introduces the existence of anisotropic fluorescence due to excitation of Cherenkov light. This hypothesis should be studied more closely to understand the possible impact for events at the Pierre Auger Observatory. At the end of this analysis, the most probable explanation for the features is a mix of the mentioned ideas which all

seem to contribute. Whatever the origin of these peculiarities is, solving this riddle has the potential to affect almost all the Auger results as well as the results of other UHECR experiments and thus the observed feature remains an exciting topic for further studies.

A Appendix

A.1 CORSIKA steering card

An official example steering card as input file for an air shower simulation which is also used for the Naples database. Each line contains the parameter name, one or multiple values and a short description. For E, Θ and ϕ a range of potential values can be declared. By setting the minimum and maximum value equal, a dedicated simulation with specific energies and geometries is possible.

Listing 1: Example steering card

```
RUNNR   1                          run number
NSHOW   1                          number of showers in run
PRMPAR  14                         primary particle type: 14=proton
ESLOPE  -1                         slope of primary energy spectrum
ERANGE  Emin   Emax                energy range [GeV]
SEED    102698 0 0                 MC seed
SEED    400231 0 0
SEED    630781 0 0
DIRECT  /
THIN    1.0E-06 1700 10000         thinning parameters
THINH   1 100                      hadronic thinning
THETAP  Zenmin  Zenmax             range of zenith angle [degree]
PHIP    Phimin  Phimax             range of azimuth angle [degree]
ATMOD   21                         atmospheric model
OBSLEV  1.452E+5                   observation level [cm]
MAGNET  20.39   -14.22             magnetic field Malargue
ECUTS   0.1 0.1 2.5E-4 2.5E-4      energy cuts for particles
MUADDI  T                          additional info for muons
MUMULT  T                          muon multiple scattering angle
ELMFLG  F   T                      em. interaction flags (NKG,EGS)
STEPFC  1.0                        mult. scattering step length fact.
RADNKG  5.0E+5                     outer radius for NKG lat.dens.distr.
LONGI   T  5.  T  T                long.distr.,step size,fit & out
ECTMAP  2.5E+5                     cut on gamma factor for printout
MAXPRT  1                          max. number of printed events
DATBAS  T                          write .dbase file
USER    user
PAROUT T T                         particle file output
EXIT                               terminates input
```

A.2 Cuts

Listing 2: LongXmax cuts

```
eyeCut                          1111
badFDPeriodRejection
minBackgroundRMS                17
!badPixels                      1
!isCLF
!isXLF
good10MHzCorrection
hasMieDatabase
maxVAOD                         {params: .1 nMinusOne: 100  0.  1.}
skipSaturated
hybridTankTrigger               2
xMaxInFOV                       0.0
maxCoreTankDist                 1500
ambiguousHybridRejection
maxZenithFD                     90
cloudCut
minLgEnergyFD                   17.8
minPBrass                       0.95
FidFOVICRC13prel
xMaxObsInExpectedFOV            40 20
maxDepthHole                    20
profileChi2Sigma                2.25 -1.1
depthTrackLength                300
```

Cuts used in the LongXmax paper [14]. These cuts focus on a precise measurement of the parameter $X_{\max}$ and are commonly used to find high quality events. Precuts include for example a hardware cut (which checks whether the PMTs and cameras working properly) and a VAOD (see Sec. 4) cut. A correct measurement of the attenuation due to aerosols is only possible within an hour around the time of the event since the aerosol content in the atmosphere can be variable on short time-scales [67]. The optical depth is integrated from the ground up to 3 km above Earth and events are only accepted for values below 0.1. Additionally all events with energies below $10^{17.8}$ eV are rejected.
The quality and fiducial cuts were initially used to get an unbiased $X_{\max}$ distribution with minimal distortions, but of course the resulting set can also be used for examining other parameters. *xMaxInFOV* requires the shower maximum to

be in the detector field of view to guarantee a more precise Gaisser-Hillas fit. Since clouds can block the light sometimes there are large gaps in the detected profile. *maxDepthHole* confines these gaps to 20% of the observed track, which has to have a length of at least 300 g/cm^2 as indicated by *depthTrackLength*. One of the most important cuts, *xMaxObsInExpectedFOV*, sets the uncertainty of $X_{\mathrm{max}} \leq 40$ g/cm^2 and the minimum viewing angle θ_{vm} to 20°, thus rejecting events with high Cherenkov fractions.

References

[1] V.Hess and W.Kolhoerster. *Über Beobachtungen der durchdringenden Strahlung bei sieben Freiballonfahrten.* Phys. Zeits., 1912.

[2] S.Cecchini and M.Spurio. *Atmospheric muons: experimental aspects.* arXiv:astro-ph/1208.1171v1, 2012.

[3] S.P.Swordy et al. Sci. Amer. v276, p.44, 1997.

[4] A.Haungs. *Cosmic Rays from the Knee to the Ankle.* arXiv:astro-ph.HE/1504.01859v1, 2015.

[5] T.Antoni et al. (KASCADE Collab.). *KASCADE measurements of energy spectra for elemental groups of cosmic rays: Results and open problems.* Astropart. Phys. 24, 1-25, 2005.

[6] S.F.Berezhnevetal et al. (Tunka Collab.). *Elemental Composition of Cosmic Rays above the Knee from the Xmax measurements of the Tunka Array.* 33rd ICRC 2013.

[7] R.Abbasi et al. (IceCube Collab.). *IceTop: The surface component of IceCube.* Nucl. Instrum. Meth. A 700, arXiv:astro-ph.IM/1207.6326, 2013.

[8] T.Abu-Zayyad et al. (TA Collab.). *Energy Spectrum of Ultra-High Energy Cosmic Rays Observed with the Telescope Array Using a Hybrid Technique.* arXiv:astro-ph.HE/1305.7273v1, 2013.

[9] R.Abbasi et al. (HiRes Collab.). *First Observation of the Greisen-Zatsepin-Kuzmin Suppression.* Phys. Rev. Lett. ,100, 2008.

[10] B.Dawson et al. *The energy spectrum of cosmic rays at the highest energies.* EPJ Web of Conferences 53, 01005, 2013.

[11] G.T.Zatsepin and V.A.Kuz'min. *Upper Limit of the Spectrum of Cosmic Rays.* Sov. J. Exp. Theor. Phys. Lett., 4, 1966.

[12] P.M.Bauleo and J.R.Martino. *The dawn of the particle astronomy era in ultra-high-energy cosmic rays.* Nature 458, 847-851, 2009.

[13] D.J.Bird et al. (HiRes Collab.). *Detection of a cosmic ray with measured energy well beyond the expected spectral cutoff due to cosmic microwave radiation.* Astrophys. Journ., 441, 1995.

[14] A.Aab et al. (Auger Collab.). *Depth of Maximum of Air-Shower Profiles at the Pierre Auger Observatory: Measurements at Energies above* $10^{17.8}$ *eV.* arXiv:astro-ph/1409.4809v3, Phys.Rev. D90 12, 2014.

[15] J.S.George et al. *Elemental composition and energy spectra of galactic cosmic rays during solar cycle 23.* Astrophys. Journ., 698, 2009.

[16] P.Auger et al. *Extensive cosmic showers in the atmosphere containing ultra-penetrating particles.* C. R. Acad. Sci. Ser. II,206, 1938.

[17] T.K.Gaisser and A.M.Hillas. Proc. 15th ICRC, 1977.

[18] W.Heitler. *Quantum theory of radiation.* Oxford University Press, 1944.

[19] S.Müller. *A Novel Method of Determining the Energy Scale of the Pierre Auger Observatory.* Diploma thesis, Karlsruhe Institute of Technology, 2008.

[20] F.Arqueros et al. *Air fluorescence relevant for cosmic-ray detection - summary of the 5th fluorescence workshop, el escorial 2007.* Nuclear Instruments and Methods in Physics Research A 597, 2008.

[21] A.Obermeier. *The Fluorescence Yield of Air excited by Electrons measured with the AirFly Experiment.* Master's thesis, Karlsruhe Institute of Technology, 2006.

[22] J.V.Jelley. *Cerenkov Radiation and its applications.* Pergamon Press, 1958.

[23] V.P.Zrelov. *Cherenkov radiation in high-energy physics.* IPST, 1970.

[24] I.Bekman. *Measurement of Cherenkov light with the HEAT telescopes at the Pierre Auger Observatory.* Master's thesis, RWTH Aachen, 2012.

[25] J.Pekala. *Atmospheric scattering of light emitted by extensive air showers.* Ph.D. thesis, University of Krakow, 2007.

[26] I.M.Frank and I.E.Tamm. Comptes Rendus Acad. Sciences U.S.S.R., 14, 1937.

[27] Y.Timofeev. *Theoretical Fundamentals of Atmospheric Optics.* Cambridge International Science Publishing Ltd., 2008.

[28] B.Valeur. *Molecular Fluorescence: Principles and Applications.* Wiley-VCH, 2001.

[29] T.J.L.McComb et al. *Polarization of Cerenkov radiation from large cosmic ray showers.* 16th International Cosmic Ray Conference, Vol. 9, 53-55, 1979.

[30] V.Gokhale et al. *Examining the feasibility of air shower core-location from polarization properties of associated Cherenkov light.* Kluwer Academic Publishers, 2001.

[31] K.Bernlöhr et al. *Measurement of the Cherenkov light spectrum and of the polarization with the HEGRA-IACT-system.* ICRC11, arXiv:astro-ph/0107149v2, 2001.

[32] A.Lang. *Time Calibration of the Auger Engineering Radio Array (AERA) Using Airplanes.* Diploma thesis, Karlsruhe Institute of Technology, 2014.

[33] L.Valore. *Atmospheric Aerosol Attenuation Measurements at the Pierre Auger Observatory.* arXiv:astro-ph/1402.6186v1, 2013.

[34] J.Abraham et al. (Auger Collab.). *Trigger and Aperture of the Surface Detector Array of the Pierre Auger Observatory.* Nucl. Instrum. Methods A 613, p.29-39, 2010.

[35] J.Abraham et al. (Auger Collab.). *The fluorescence detector of the Pierre Auger Observatory.* Nuclear Instruments and Methods in Physics Research A 620, p. 227-251, 2010.

[36] J.Abraham et al. (Auger Collab.). *Properties and performance of the prototype instrument for the Pierre Auger Observatory.* Nuclear Instruments and Methods in Physics Research A 523, p. 50-95, 2004.

[37] F.Salamida. *Update on the measurement of the CR energy spectrum above* 10^{18} *eV made using the Pierre Auger Observatory.* 32rd ICRC, Beijing, 2011.

[38] A.Letessier-Selvon. *Highlights from the Pierre Auger Observatory.* 33rd ICRC, Rio De Janeiro, 2013.

[39] C.Meurer and N.Scharf. *HEAT - a low energy enhancement of the Pierre Auger Observatory.* Proceedings of 22nd European Cosmic Ray Symposium (ECRS 2010), 2011.

[40] B.Fuchs et al. *The Auger Engineering Radio Array.* Nuclear Instruments and Methods in Physics Research A, 692, pp. 93-97, 2012.

[41] J.Neuser. *Radio Measurement of Extensive Air Showers at the Pierre Auger Observatory.* Master's thesis, Bergische Universität Wuppertal, 2010.

[42] F.Schröder. *Radio detection of air showers with the Auger Engineering Radio Array.* Proceedings of 33rd International Comic Ray Conference (ICRC13), 2013.

[43] D.Heck and T.Pierog. *Extensive Air Shower Simulation with CORSIKA: A User's Guide.* Karlsruhe Institute of Technology, 2013.

[44] NOAA Magnetic field calculator. `http://www.ngdc.noaa.gov/geomag-web/#igrfwmm`. [Online; accessed 23. September 2015].

[45] M.Grigat. *Large Scale Anisotropy Studies of Ultra High Energy Cosmic Rays Using Data Taken with the Surface Detector of the Pierre Auger Observatory.* Ph.D. thesis, RWTH Aachen, 2011.

[46] S.Argiro et al. *The Offline Software Framework of the Pierre Auger Observatory.* arXiv:astro-ph/0707.1652v1, 2007.

[47] I.C.Maris et al. *Utilities for ADST-Analysis.* Karlsruhe Institute of Technology, 2009.

[48] H.P.Dembinski. *Measurement of the flux of ultra high energy cosmic rays using data from very inclined air showers at the Pierre Auger Observatory.* Ph.D. thesis, RWTH Aachen, 2009.

[49] M.Unger. *Shower Profile Reconstruction from Fluorescence and Cherenkov light.* GAP-2006-010.

[50] V.Novotny et al. *Accuracy of shower parameters in stereo reconstruction.* GAP-2013-110.

[51] A.Porcelli. *Measurement of the Depth of Shower Maximum in the Transition Region between Galactic and Extragalactic Cosmic Rays with the Pierre Auger Observatory.* Ph.D. thesis, Karlsruhe Institute of Technology, 2014.

[52] P.Homola. Mass composition teleconference, 2014.

[53] F.Guarino et al. (Naples shower library). `http://natter.na.infn.it:18501/se02a1/ReadADST/v2r9p5/`, 2015. [Online; accessed 23. September 2015].

[54] J.Parrisius. *Test of the calibration of the Auger fluorescence telescopes with an isotropic UV light source.* Diploma thesis, Karlsruhe Institute of Technology, GAP-2009-045.

[55] V.Verzi. *The Energy Scale of the Pierre Auger Observatory.* 33rd ICRC 2013.

[56] L.Niemietz. *Pixel-by-Pixel calibration for the Pierre Auger fluorescence telescopes.* Diploma thesis, Bergische Universität Wuppertal, 2010.

[57] M.Unger et al. *Simulation of the Point Spread Function of the FD Telescopes and its Effect on the Reconstructed Energy and X_{max}.* GAP-2013-069.

[58] B.Dawson et al. *Proposal for an update of the Auger Energy Scale.* GAP-2012-124.

[59] J.Rautenberg. private communication, 2015.

[60] P.Homola et al. *Asymmetry of the angular distribution of Cherenkov photons of extensive air showers induced by the geomagnetic field.* Astroparticle Physics 60, p. 47-53, 2015.

[61] I.Jandt et al. *International Geomagnetic Reference Field implemented into Offline.* GAP-2014-96.

[62] F.Nerling et al. *Universality of electron distributions in high-energy air showers - description of Cherenkov light production.* Astropart.Phys.24:421-437, 2006.

[63] M.Giller and G.Wieczorek. *Influence of the scattered Cherenkov light on the width of shower images as measured in the EAS fluorescence experiments.* Astropart.Phys.31:212-219, 2009.

[64] P.Homola. private communication, 2015.

[65] The Pierre Auger Collaboration. *The effect of the geomagnetic field on cosmic ray energy estimates and large scale anisotropy searches on data from the Pierre Auger Observatory.* Journal of Cosmology and Astroparticle Physics 022, 2011.

[66] M.Unger et al. `https://web.ikp.kit.edu/munger/Xmax/`. [Online; accessed 23. September 2015].

[67] R.Cester et al. *Atmospheric aerosol monitoring at the Pierre Auger Observatory.* 29th ICRC, Pune, 2005.

Danksagung

An dieser Stelle möchte ich allen danken, die mir in irgendeiner Art und Weise bei der Erstellung dieser Arbeit behilflich waren.
An erster Stelle danke ich Prof. Karl-Heinz Kampert für die Gelegenheit an diesem faszinierenden Projekt mitzuarbeiten und meine Arbeit zu betreuen. Weiterer Dank geht an Prof. Klaus Helbing und seine Bereitschaft als Koreferent zu fungieren.
Chcę wyrazić moją niezmierną wdzięczność Piotrowi Homole. Przez twój entuzjazm i inspirację w związku z tematem, bardzo nam pomogłeś.
Ein besonderer Dank geht an Julian Rautenberg, der mit seinem breiten Allgemeinwissen über alles was zum Pierre Auger Experiment dazugehört einen wertvollen Beitrag lieferte. Meinem Bürokollegen Philipp Papenbreer danke ich für die gute Arbeitsatmosphäre und das Beantworten vieler kleiner und auch größerer Fragen die sich während des Arbeitens ergaben. Ich danke Tobias Winchen für die technische Unterstützung, besonders zu Beginn meiner Arbeit.
Desweiteren möchte ich der Gruppe um Fausto Guarino und Roberta Colalillo aus Neapel für die Bereitstellung einer hochqualitativen Bibliothek an simulierten Schauern danken. Die Fertigstellung der erneuten Rekonstruktionen so kurz vor Ende meiner Bearbeitungszeit erlaubte es mir die wissenschaftliche Aussagekraft der Arbeit erheblich zu steigern.
Ein großer Dank geht an Vladimír Novotný für seine ausführliche Hilfe bezüglich der Verarbeitung der simulierten Datensets.
Schließlich danke ich sowohl meiner Familie als auch Melina für Verständnis und Unterstützung im gesamten Verlauf meines Studiums.

Eidesstattliche Erklärung

Hiermit versichere ich, dass ich die Arbeit selbstständig verfasst, keine anderen als die angegebenen Quellen und Hilfsmittel benutzt sowie Zitate kenntlich gemacht habe.

Wuppertal, den _____ _____

(Unterschrift)